THE THERMAL CONDUCTIVITY OF LaF_3:0.1%Er^{3+} FROM 1.8 K TO 100 K

By

WAYNE W. VINSON

Bachelor of Science
Panhandle State University
Goodwell, Oklahoma
1973

Master of Science
Oklahoma State University
Stillwater, Oklahoma
1977

Submitted to the Faculty of the Graduate College
of the Oklahoma State University
in partial fulfillment of the requirements
for the Degree of
DOCTOR OF PHILOSOPHY
May, 1987

Thesis
1987D
V788t
cop.2

OKLAHOMA STATE UNIVERSITY LIBRARY

THE THERMAL CONDUCTIVITY

OF LaF_3:0.1%Er^{3+} FROM

1.8 K TO 100 K

Thesis Approved:

George S. Viefhaus
Thesis Adviser

Timothy M. Wilson

Joel T. Martin

M. E. Rockley

Norman N. Durham
Dean of the Graduate College

1286908

PREFACE

The thermal conductivity of CaF_2 and LaF_3 doped with 0.1 percent erbium was measured as a function of temperature from 1.8 K to 100 K. The curves obtained were fit using a Debye formulation for the thermal conductivity, where the phonon-phonon relaxation times used were deduced from those obtained by other phonon spectrographic methods. The results of this procedure were used to predict the anharmonic decay rates for several other materials.

I wish to express my sincere gratitude to all the people who assisted me in this work and during the period of time I have spent here at Oklahoma State University.

It is with particular sincerity that I express my gratitude to my major thesis advisor, Dr. George S. Dixon for his patience, understanding, and guidance throughout all my graduate studies, as well as in this thesis effort.

I am also thankful for technical and advisory support from the members of my committee, Dr. Timothy M. Wilson, Dr. Mark G. Rockley, and Dr. Richard C. Powell. Special thanks are due to Dr. Larry Halliburton and Dr. Joel Martin for advice and technical assistance which led to the timely completion of this work.

Special thanks are due also to Mr. Heinz Hall for his technical skills in the construction of equipment, and to Renea Behrens for her patience and skill in preparing the manuscript of the thesis.

I also express my deepest appreciation to my wife, Cathy, and my

children, John, Crystal, Matthew, Mark, and Sarah, for their sacrifices, support, and understanding during the whole period of my graduate studies.

Finally, I am particularly thankful for Dr. William A. Sibley's advice and encouragement, especially at the outset of this research.

TABLE OF CONTENTS

Chapter Page

LIST OF TABLES

LIST OF FIGURES

CHAPTER I

INTRODUCTION

Interest In LaF_3

Lanthanum trifluoride is a dense, colorless, dielectric solid which occurs naturally as the mineral tysonite. Its rare natural occurence is invariably in combination with a sister material, cerium trifluoride, along with trace amounts of ytterbium, neodymium, erbium, and yttrium. Samples grown in the laboratory have been used for studies since the fifties, and Stockbarger grown samples have been commercially available for several years.

Being a somewhat exotic material, consisting of heavy rare earth ions in a matrix of fluorine, it has been a subject of physical interest since its structure was reported by Oftedal [1] in 1929. Work prior to 1950 touched on few aspects of LaF_3, but after the war applied studies increased, with plutonium separation schemes dominating the field. Notable for this period was the development of preparation and purification allowing optical studies to be done, which resulted in the discovery that, along with NdF_3, LaF_3 had a featureless optical absorption spectrum, and was suitable for optical thin film applications.

Interest in LaF_3 took new directions during the sixties, and physical work concentrated on samples prepared having impurities intentionally introduced. In particular, the promise of LaF_3 as a laser host has spurred investigations into the structural, optical, and thermal

behavior of the pure material. Structurally, tysonite, shown in Figure 1, appears to be nearly hexagonal, having six molecules per unit cell, and probably belongs to the trigonal space group D_{3d}^{4} [2] [3] [4]. Questions about the Raman-spectral behavior have been partially clarified by the recent publication of the detailed vibrational dispersion relations obtained from thermal neutron scattering [5]. Perhaps more relevant to its promise as a laser host is the question of the crystal's ability to dissipate the heat generated from the lasing process itself. The principal parameter characterizing this ability is the thermal conductivity. Early measurements taken at liquid nitrogen and room temperature of the undoped material were all that were available until Hudson's 1976 work, which extended the 77 K measurements down to about 2K [6] [7]. For laser applications, though, the crystal is not "pure", but is intentionally grown with a small percentage of dopant, usually a rare-earth metal, such as erbium or neodymium, added to the starting material. The presence of these ions may significantly affect the heat flow in certain temperature ranges.

In general, the thermal properties of the doped material are not as well characterized as those of the undoped. For undoped LaF_3, the thermal conductivity as mentioned earlier is available from the literature, as is the specific heat down to around 5K [8]. The thermal conductivity of a "nominally pure" sample, grown under conditions where no special care was taken to avoid impurities, is reported by Hudson [9]. His sample exhibits unusual thermal conductivity which, he suggests, reflects the presence of large plate-like defects lying in the basal plane. He suggests the "plates" may consist of oxygen accumulations.

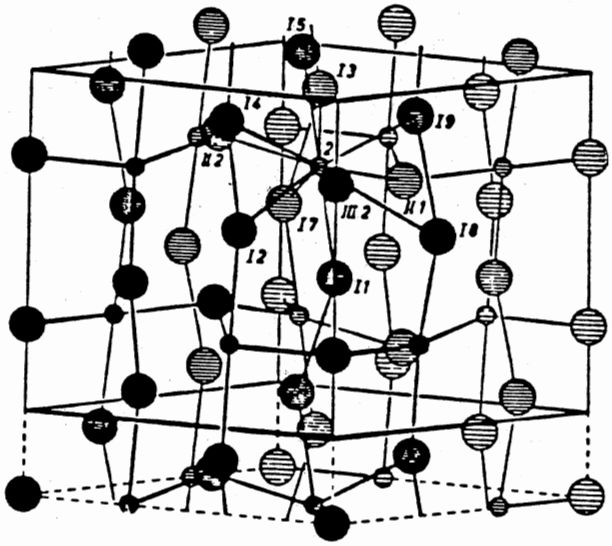

Source: 3

Figure 1. Lanthanum Trifluoride Structure

So far, the motivation for investigating the thermal conductivity of lanthanum trifluoride has been derived from fairly general considerations, but another reason supporting further study came about as a result of the neutron scattering work mentioned earlier. Figure 2, reproduced from Dixon and Nicklow [5], show the measured dispersion curves of the lowest energy lattice vibrations of a LaF_3 crystal containing 0.1% trivalent erbium. As can be seen from the figure, low frequency optical modes extend across the Brillouin zone and intersect the acoustical branches several times. This feature, a tendency in fluorides, is unusual in that most other crystalline solids have optical modes whose energies significantly exceed those of the acoustic mode, and are thus clearly above the acoustical in the dispersion mode curves except perhaps near the zone boundaries. The existence of such low-lying optical branches could provide an additional scattering mechanism not seen in crystals with "normal" dispersion relations.

General Properties of LaF_3

Most of the basic physical properties relevant to the present study of crystalline lanthanum triflouride are available from the literature. Sound velocities of the acoustic lattice modes were obtained by Laiho, Lakkisto, and Lavola [10] with Brillouin scattering measurements and from these, elastic constants were determined assuming a hexagonal structure. Their measurements for the tranverse sound velocity are in agreement with those of Krischer [11] obtained from Bragg diffraction of coherent light by ultrasonic waves. Low temperature specific heat for LaF_3 is available from Lyon et. al. [7], who did calorimetric measurements on a 100 gram powder sample loaded into a gold-plated copper

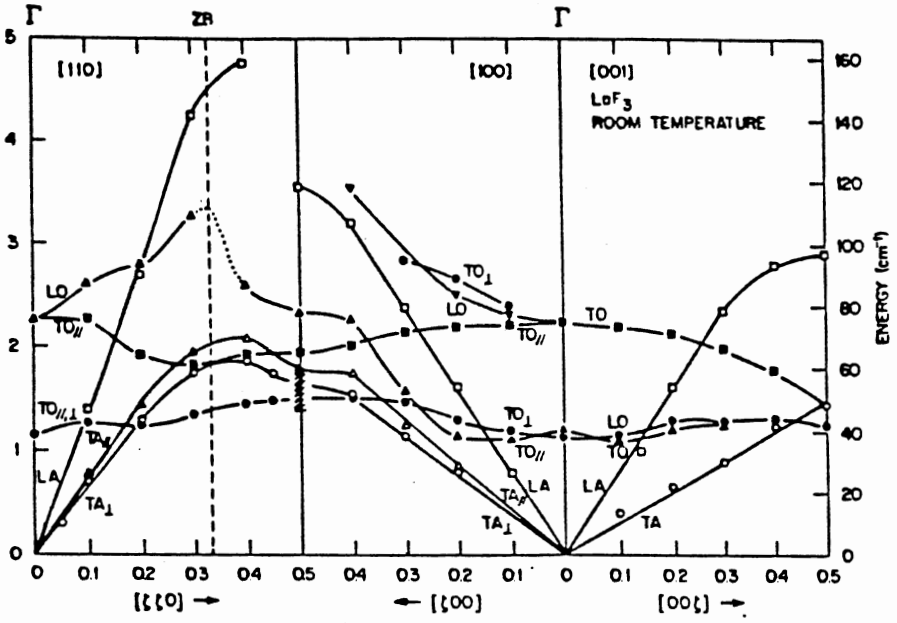

Source: 5

Figure 2. Phonon Dispersion Relations for LaF_3

calorimeter. Although the authors modelled the section between 120 K and 280 K of the specific heat curve with a Debye temperature of 450 K, a plot using their values against T for Θ_D = 400 K produces a curve approaching C_p = 100 J/mole°K = 12R in the high temperature limit. This lower value for the Debye temperature is closer to the 385 K value obtained by Laiho, et al., in their work. An unusual feature of the results of Lyon et al. and also by Westrum and Beale [12] on isostructural CeF_3 is that the low temperature heat capacities of both materials fall off faster than T^3: $T^{3.5}$ for LaF_3; $T^{3.3}$ for CeF_3. Whether these are artifacts of the experimental procedure or intrinsic properties of the samples is not apparent, although such behavior may be due to low optic mode contributions.

Thermal conductivity measurements from Hudson [6] are reproduced in Figure 3, and represent the variation with temperature of the nominally pure material. As for most crystals, the thermal conductivity is higher at a given temperature for transport parallel to the highest symmetry direction, if one exists, than in other directions. The curve is characteristic of those of many crystalline solids in that the maximum occurs around 10K and decreases because of the drop in specific heat for temperatures below that of the maximum and because of the decrease in the mean free paths of the phonons for temperatures above it.

Additional information about phonon transport in LaF_3 has been obtained through the use of optical techniques of phonon spectroscopy. Recenty, K. Renk's group in Regensburg [13], has determined lifetimes of terahertz phonons against anharmonic decay at low temperatures. These results are discussed in more detail in Chapter II, and will be related to thermal conductivity in an approximate manner.

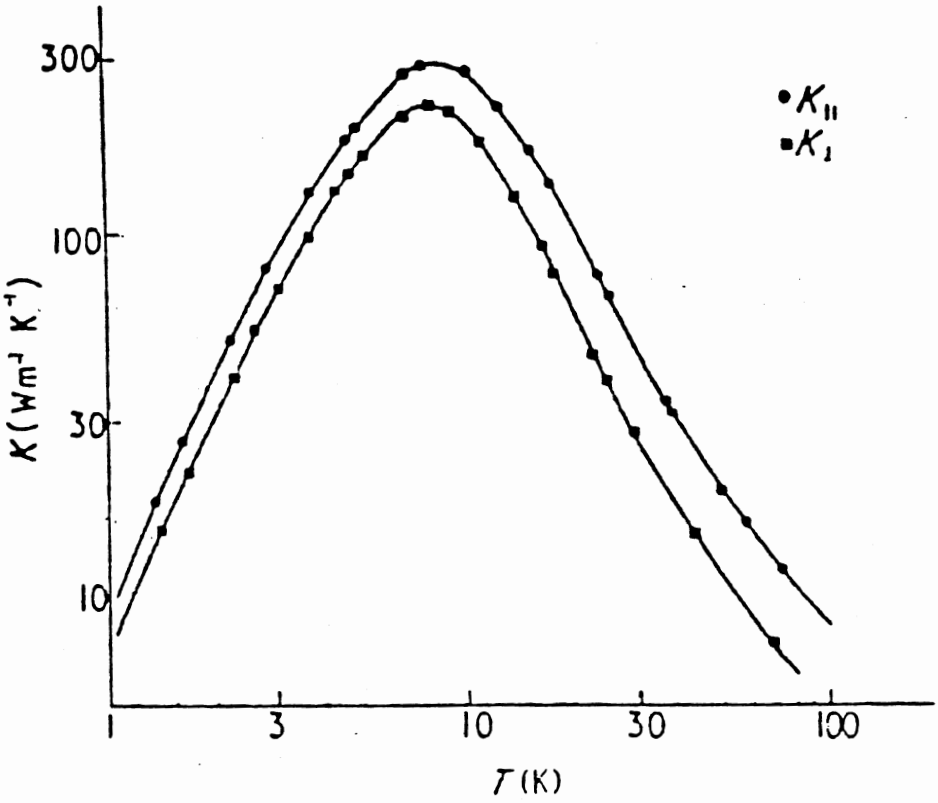

Source: 6

Figure 3. Principal Thermal Conductivities of LaF_3

Interest in CaF_2

Like LaF_3, fluorite has been a subject of study for many years. Its crystal structure, shown in Figure 4, is simpler, being simple cubic where each Ca atom has eight fluorine atoms as nearest neighbors. Each unit cell contains one molecule of three atoms each, giving nine phonon branches, three acoustic and 33 optic. From the phonon dispersion curve obtained by thermal neutron diffraction [14] shown in Figure 5, one can see that the transverse branches are degenerate or nearly so in three principal directions. Table I summarizes CaF_2 and LaF_3 data.

There are two reasons CaF_2 has been included in this study. Primarily, it was intended, since its thermal conductivity has been well characterized, to serve as a check on the accuracy of the experimental method [15] [16] [17]. Secondly, it also serves as a host for rare earth ions and has been a subject of phonon spectroscopy investigations of anharmonic decay, as has LaF_3. So it would be fruitful to analyze the CaF_2 data as well.

Thermal Conductivity of Dielectric Crystals

General

Heat conduction in dielectric and most semiconducting solids is due to lattice vibrational transport. Thermal resistivity, conversely, is a consequence of the presence of factors which either separately or in combination serve to hinder this transport. Examination of experimental results reveals that, among dielectrics, any crystalline form of a solid conducts heat better, even as much as ten times better, than its chemically identical non-crystalline form, and further, that the totally

TABLE I

SUMMARY OF DATA FOR LaF_3 AND CaF_2

	$\bar{v}_t$	$\bar{v}_t$	$\bar{v}_\ell$	$\bar{v}^*$	Θ_D	Θ_D(spec. heat)	ρ	a_o^3
	(km/s).....				(K)	(K)	(gm/cm^3)	(A^3)
LaF_3	6.0	2.7	2.4	3.0	385	400	5.9	282
CaF_2	7.8	3.9	3.5	4.1	505	514	3.2	163

* The determination of $\bar{v}$ is detailed in Appendix H.

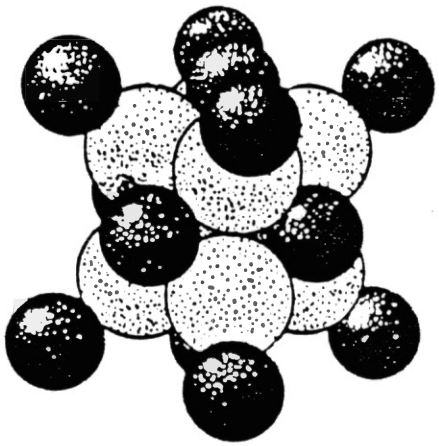

Source: 18

Figure 4. Calcium Fluoride Structure

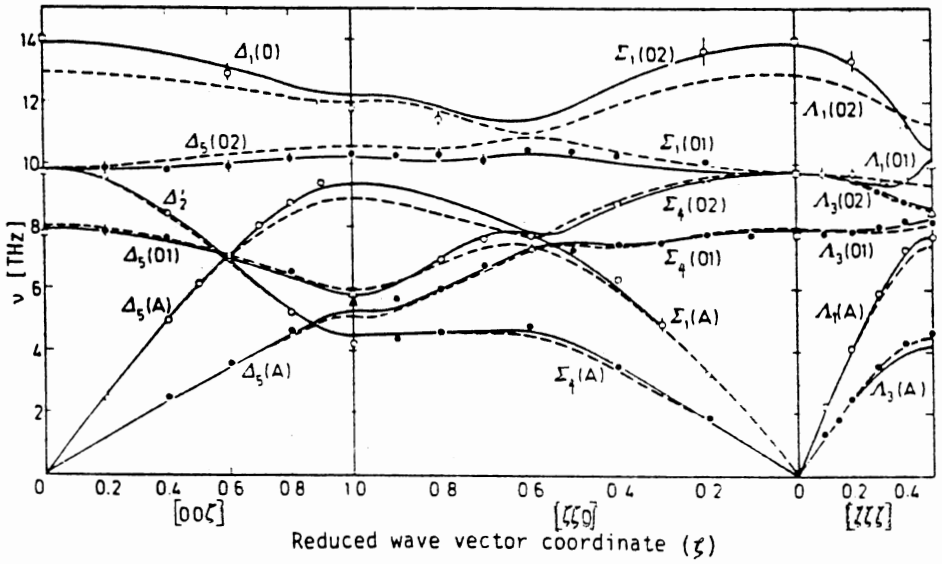

Source: 14

Figure 5. Phonon Dispersion Relations for CaF_2

amorphous sample is a poorer conductor than its polycrystalline counterpart. Naturally, this observation suggests that the degree of symmetrical ordering of atoms comprising the solid is one major determinant of a given material's capacity to conduct heat. In addition, comparisons among different, yet ostensibly pure, crystalline solids show thermal conductivity variations which reflect dependence on bonding strength, dependence on structure, and temperature dependence which, apart from a scale factor in the first approximation, shows great similarity from sample to sample.

Beyond such generalities, further description of thermal transport becomes impossible without delving into the details of the atomic vibrations responsible for transport; the nature of the inhomogeneitics responsible for resistivity; and the kinetic theory of transport described by the Boltzmann equation, whose solutions may model the steady states attained by the above competing processes.

The Thermal Conductivity

The parameter used to describe a material's ability to transport heat in a steady state situation is known as the thermal conductivity, denoted here as λ, and has the units of power per unit length per temperature. Its MKS units are watt/(meter K). Macroscopically, for an isotropic solid, the thermal conductivity is defined by Fourier's Law

$$\vec{J} = dQ/dt = -\lambda \vec{\nabla} T \qquad (1)$$

where $\vec{J}$ (or $\dot{\vec{Q}}$) is a vector quantity which measures the rate of heat flow across a unit area due to a spatial gradient of temperature. In the nonisotropic case the thermal conductivity is represented as a

tensor λ_{ij} where

$$J_i = -\Sigma_j \lambda_{ij} \frac{\partial T}{\partial x_j} \tag{2}$$

For a steady state experimental situation where the cross-sectional area, A, of the sample is a constant along a length L, which separates a pair of thermometers, Equation (1) reduces to

$$J = -\lambda A \frac{\Delta T}{L} \tag{3}$$

and if the flux J is constant, $\lambda = \frac{WL}{A\Delta T}$, where W is the power.

The rise in temperature of a given portion of a dielectric is dependent upon how much the internal (lattice vibrational) energy is increased, and therefore, is a function of that material's specific heat. Equations (1-3) describe the flow of heat modelled as diffusion and since, from a continuity equation

$$\frac{\partial \rho}{\partial t} = -\vec{\nabla} \cdot \vec{J} \tag{4}$$

where ρ is an "energy density", and if $d\rho = C_v dT$ equation (1), rewritten as

$$\vec{J} = -a^2 \vec{\nabla} \rho \tag{5}$$

becomes

$$\frac{\partial \rho}{\partial t} = -\vec{\nabla} \cdot (-a^2 \vec{\nabla} \rho) = a^2 \nabla^2 \rho$$

or $$\frac{\partial T}{\partial t} = a^2 \frac{\partial^2 T}{\partial x^2} \tag{6}$$

which is the diffusion equation.

This equation gives the correct behavior of macroscopic heat flow

through a solid once the thermal conductivity and specific heat are known but sheds no illumination on the dependence of the conductivity upon the fundamental properties of a solid.

Therefore, to obtain qualitative and, hopefully, some quantitative understanding one must construct more realistic models of crystals, in which the transport of heat energy is due entirely in dielectrics to the vibrations of its atoms (except in the case of magnetically ordered materials at very low temperatures). If a pure solid is modeled as an elastic continuum, the establishment of equilibrium from a thermal perturbation is not possible [19]. This comes about because wavevector conservation laws inherent in the model make it impossible to destroy a heat current once it is established. One must treat the vibrations of a disordered array of atoms explicitly to account for resistivity. Although the vibrational modes are correctly given by classical theory, a more physical model is obtained by quantization of the motion. The classical picture of energy distribution among normal modes as measured by atomic displacement amplitudes is replaced by a picture whereby the energy is distributed among a large number of linearly independent stationary states in descrete quanta of $\hbar\omega$. This procedure replaces lattice waves with quantum particles known as phonons, and transforms the problem of energy flow due to wave motion to a problem of transport of a gas of phonons. Unlike real gas particles, though, phonons carry no real momentum, are not number-conserved, are polarized, reflect anisotropy of direction, are subject to dispersion, have finite lifetimes, and obey Bose-Einstein statistics. In principle, one may state that whatever conditions in a crystal that limit phonon lifetimes, change their number, their direction, or their velocity will contribute

to thermal resistivity. These include structural imperfections, point defects, other phonons and sample boundaries.

Thus, one may state that energy transport in a crystalline dielectric is largely due to phonons. If the phonons generated are from one or a small number of modes, the energy is propagated as an ultrasonic wave. If these modes are excited to such an extent that the energy of this group of modes is much higher than the total energy, in thermal equilibrium, of all the other modes, and ultrasonic beam results, whose attenuation in space or time can be studied. Such phonons have small wavevectors, large mean free paths, and being more or less in phase, are regarded as coherent.

On the other hand, if the crystal is heated non-uniformly, the phonons created are generally distributed among modes having no phase relationship, and are regarded as incoherent. The frequency of the highest energy ultrasonic mode is on the order of two orders of magnitude below that of ordinary thermal phonons, and this accounts for the very large difference in their mean free paths for a given temperature. Thermal phonons have much shorter paths because they are more sensitive to perturbations of crystal periodicity and are more subject to scattering. Because of the difficulty in efficiently coupling ultrasonic transducers to crystals, one is limited to frequencies less than 10 GHz by this technique. However, the most important thermal phonons, even at 10K, have $\omega/2\pi > 100$GHz. Such phonons propagate diffusively and their scattering mechanisms are studied through obtaining and analyzing the thermal conductivity as a function of temperature (and possibly other factors). Until recent studies of the evolution of phonon distributions by the heat pulse and other methods, thermal conductivity provided

nearly the only information concerning phonon scattering in the terahertz region [20].

Modeling Thermal Conductivity

Since the complete solution of the fully interacting phonon system in the nonequilibrium situation is not presently obtainable, one must resort to approximations and models. Transport problems are often modeled with a (linearized) form of the Boltzmann Equation in which one assumes that scattering processes tend to restore a phonon distribution to thermal equilibrium at a rate proportional to its departure from equilibrium. In other words, the system returns to equilibrium exponentially with time. Mathematically

$$\left(\frac{\partial N}{\partial t}\right)_{\text{scattering}} = -\frac{N-N_o}{\tau} \tag{8}$$

where N is the phonon number, N_o is the equilibrium phonon occupation number, and τ is defined as the relaxation time. If one considers phonons of lifetime τ, wavevector q, polarization p, as carriers of heat, then the heat flow may be written

$$\vec{J} = \Sigma_{qp} N_q \hbar\omega_{p,q} v_{p,q} \tag{9}$$

where $v_{p,q}$ is the group velocity of a phonon in branch p having a wavevector $\vec{q}$.

The distribution in the presence of the temperature gradient is a result of diffusion processes and scattering processes. Phonons enter and leave a volume of the crystal due to their velocities and can be written

$$\left(\frac{\partial N_q}{\partial t}\right)_{\text{diff}} = -\vec{v}_q \cdot \vec{\nabla} N_q \tag{10}$$

Scattering processes change the population of the $\vec{q}$-states, and the total change in the distribution can be written

$$\left(\frac{\partial N_q}{\partial t}\right)_{total} = \left(\frac{\partial N_q}{\partial t}\right)_{diff} + \left(\frac{\partial N_q}{\partial t}\right)_{scatt} \tag{11}$$

In steady state conditions $(\partial N_q/\partial t)_{total} = 0$ so that

$$\left(\frac{\partial N_q}{\partial t}\right)_{diff} = -\left(\frac{\partial N_q}{\partial t}\right)_{scatt} \tag{12}$$

In the absence of a temperature gradient there is no net change in N_q as a consequence of diffusion so that $(\partial N_q/\partial t)_{diff} = -(\partial N_q/\partial t)_{scatt} = 0$ and $N_q = N_q^\circ$, where N_q° is the equilibrium distribution. On the other hand, if a temperature gradient is present, the distribution N_q can be regarded to deviate by a small amount from a local equilibrium, $N_q(\vec{r})$, distribution and is determined by the temperature at $\vec{r}$ [21], then

$$\vec{v}_{p,q} \cdot \vec{\nabla} N_q(\vec{r}) = \vec{v}_{p,q} \cdot \frac{\partial N_q^\circ}{\partial T} \vec{\nabla} T \tag{13}$$

For the case of elastic scattering, the linearized Boltzmann Equation has the solution

$$N_q - N_q^\circ = -\vec{v}_{p,q} \cdot \frac{\partial N_q^\circ}{\partial T} \vec{\nabla} T \tau_q \tag{14}$$

where τ_q is the relaxation time for the scattering process. Then the heat current, Eq. (9) can be written

$$\vec{J} = \Sigma_{q,p} \{N_q^\circ - \vec{v}_{p,q} \cdot \frac{\partial N_q^\circ}{\partial T} \vec{\nabla} T \tau_q\} \hbar\omega_{p,q} \vec{v}_{p,q} \tag{15}$$

Since $N_q^\circ = N_{-q}^\circ$, $\omega_{p,q} = \omega_{p,-q}$, and $v_{p,q} = -v_{p,-q}$, the first sum on the right hand side vanishes and

$$\vec{J} = -\nabla T \cdot \Sigma_{q,p} \{-\vec{v}_{pq} \tau_q \frac{\partial N_q^\circ}{\partial T} \hbar\omega_{p,q} \vec{v}_{p,q}\} \tag{16}$$

$$J_i = -\Sigma_{p,q} \Sigma_j \frac{\partial T}{\partial x_j} v_i v_j \tau_q \frac{\partial N_q}{\partial T} \hbar\omega_{p,q} = -\Sigma \lambda_{ij} \frac{\partial T}{\partial x_i}$$

$$\text{with} \quad \lambda_{ij} = \Sigma_{p,q} v_i v_j \tau_q \frac{\partial N_q^o}{\partial T} \hbar\omega_{s,p} \tag{17}$$

In one dimension,

$$\lambda_{ij} = \lambda_{ii} = \lambda_i = \Sigma_{p,q} v_i^2 \tau_q \frac{\partial N_q^o}{\partial T} \hbar\omega_{p,q} \tag{18}$$

If one writes $v_i^2{}_{p,q} = \frac{1}{3} v_{p,q}^2$, and letting $\Sigma \to \int f(\vec{q}) d\vec{q}$

$$\lambda = \frac{1}{3} \Sigma_p \int d\vec{q} v_p^2(q) \tau_p(q) \hbar\omega_p(q) f(\vec{q}) \frac{\partial N(q)}{\partial T} \tag{19}$$

where $f(q)$ is the density of states.

To actually calculate this integral using the frequency spectrum and dispersion relations of a real crystal would be a formidable task even if they were known, because of the difficulties involved in determining $\tau(q)$ in detail. Generally, the thermal conductivity is calculated from the simpler formulation given by the Debye model. This model postulates $\omega_p(\vec{q}) = v_{pq}$ for each branch of the phonon spectrum. Since for a Bose-Einstein distribution

$$N_q^o = [\exp(\hbar\omega_p(q)/kT) - 1]^{-1} \tag{20}$$

Then

$$\frac{\partial N_q^o}{\partial T} = \frac{(\hbar\omega(q)/kT)\exp(\hbar\omega_p(q)/kT)}{[\exp(\hbar\omega_p(q)/kT)-1]^2} \tag{21}$$

For the density of states one has, for acoustic branches,

$$f(q)dq = \frac{Vq^2 dq}{2\pi^2 v_p} \tag{22}$$

which, since $\omega_p = v_p q$ in the Debye model,

$$f(\omega)d\omega = \frac{V\omega^2}{2\pi^2 v^3}\, d\omega \tag{23}$$

and $$\int_0^{\omega_D} f(\omega)d\omega = 3N \tag{24}$$

where N is the number of unit cells in the crystal and r is the number of atoms per unit cell. Equation (19) becomes, when only acoustic branches are considered,

$$\lambda = \Sigma_p \frac{V\hbar^2}{2\pi^2 v^3 kT^2} \int_0^{\omega_D} \frac{\omega^4 e^{\hbar\omega/kT}}{(e^{\hbar\omega/kT}-1)^2}\, \tau(\omega)d\omega \tag{25}$$

If $x = h\omega/kT$ then

$$\lambda = \frac{k}{2\pi^2}\left(\frac{k}{\hbar}\right)^3 T^3 \Sigma_p \frac{1}{v_p} \int_0^{\hbar\omega_D/KT} \tau_p(x)\, \frac{x^4 e^x}{(e^x-1)^2}\, dx \tag{26}$$

since the specific heat in the Debye model is

$$C_p(x) = \frac{3k}{2\pi v_p^3}\left(\frac{k}{\hbar}\right)^3 T^3 \frac{x^4 e^x}{(e^x-1)^2} \tag{27}$$

then $\lambda = \frac{1}{3}\Sigma_p v_p^2 \int_0^{\omega_D} \tau_p(x)C_p(x)dx$

The value of ω_D is chosen such that Eq. (24) is satisfied, i.e.,

$$\int_0^{\omega_D} f(\omega)d\omega = \Sigma_p \int_0^{\omega_D} f(\omega)d\omega = \Sigma_p 3N = 3N \tag{28}$$

where one recalls that the subscript p denotes the separate branches of the dispersion relation. $3N_p$ represents the number of states in branch p. In this case

$$\int_0^{\omega_D} \frac{\omega^2 d\omega}{2\pi^2 v^3} = 3N \tag{29}$$

$$\omega_p = (6\pi^2 N)^{1/3} v_s \tag{30}$$

The Debye temperature is defined so that $h\omega_D/kT = \Theta_D/T$. Thus

$$\Theta_D = \hbar\omega_D/k = (\hbar/k)(6\pi N)^{1/3} v_s \tag{31}$$

In practice, the Debye temperature is sometimes determined experimentally for a given crystal to give the best fit to the specific heat data, but more commonly it is obtained from sound velocity measurements as from Brillouin scattering.

The relaxation time contains information about the specific scattering processes for phonons. If, as in actual crystals, several scattering mechanisms are operating simultaneously and incoherently, then one may add the rates for each process so $\tau_1^{-1} + \tau_2^{-1} + \ldots\tau_i^{-1} = \tau^{-1}$, where τ^{-1} represents the net rate at which phonons are scattered out of or into a given mode. Such a procedure would satisfy the condition stated by Equation (8) concerning the nature of a thermally perturbed system's return to equilibrium. In practice, phonon scattering by boundaries, point and isotopic defects, grain boundaries-in short-all resistive scattering centers allow such an approach; but phonon-phonon interactions, which are important in very pure crystals at all temperatures, and in all crystals at high temperatures, may not tend to restore a distribution according to Equation (8) because such interactions may cause intermode repopulation.

Scattering of Phonons

Because different wavelength phonons dominate the phonon distribution at different temperatures, the thermal conductivity varies with temperature. At absolute zero there are no phonons in a crystal and

atoms vibrate according to the uncertainty principle, with zero-point energy. At temperatures near 1-3 K and thermal equilibrium the phonons appear as the excited states of the lattice and their distribution is dominated by those having $\hbar\omega \sim 4kT$. Such phonons may have mean free paths on the order of centimeters if the crystal is relatively free from imperfections. When subjected to a small temperature gradient they carry energy from higher temperature regions to lower temperature regions rather efficiently, the heat transport being limited largely by their population at a given temperature and the external dimensions of the sample. As the average temperature rises, this steady, near-equilibrium, transport condition begins to reflect the introduction of more phonons of shorter wavelengths. These phonons "see" imperfections as point defects, impurities, isotopes, interstitial atoms, and the dominant phonons around 10 K are most strongly scattered by these centers. In most crystalline materials the heat transport becomes a maximum around this temperature because another effect arises to limit phonon path lengths.

At all temperatures phonons collide with each other. At low temperatures the excitations of the lattice are largely acoustic phonons having energy $\hbar\omega = vq$ where q is the phonon wavevector. When these phonons collide, the effect in the locality of the interaction is that the atoms may be driven into anharmonic regions of the interatomic pontential. When this happens the two original phonons decay, creating a new phonon having the sum of their energies and at low enough energies, the sum of their wavevectors. Also, the reverse may occur, where a thermal phonon generated in the "high" temperature region may propagate to a lower temperature region and spontaneously decay into two

phonons of lower energy and smaller wavevector. As the temperature of the sample rises these interactions become more frequent. The manner in which they limit heat transport is rather subtle, and depends upon the discrete nature of the atomic lattice, as the following argument shows.

Peierls [19], demonstrated that a phonon population governed by purely harmonic interactions would have no mechanism to limit heat transport. Further, he showed that even in the case where anharmonicity in the Hamiltonian gave rise to three phonon interactions, those collisions conserving phonon wavevector could make no such contribution. Since three phonon processes are governed by two conservation theorems

$$\omega_1 = \omega_2 + \omega_3 \tag{32}$$

$$\vec{q}_1 + \vec{q}_2 = \vec{q}_3 + \vec{G}$$

where G is a reciprocal lattice vector, there exist solutions for which wavevector conservation does not hold: cases where $G \neq 0$. Such cases occur, for example, where two phonons combine to form a single phonon, when the resultant of the vector sum of the phonons destroyed falls outside the Brillouin Zone. Such a phonon wave vector has an equivalent wavevector lying inside the Brillouin Zone, and this wavevector is obtained by adding a reciprocal lattice vector to the resultant lying outside the zone. This process always reverses the direction of the componont of the resultant lying perpendicular to the boundary of the Brillouin Zone through which it passes. But for the processes where $\vec{G} = 0$ the thermal energy is carried in the direction of the phonon group velocity, the direction of heat flow by the resultant is similar to the direction of the heat flow due to the original phonons. To show that Normal processes do not relax the heat current, note that the contri-

bution to the heat current of mode 1 is $\vec{J}_1 = \frac{n_1}{V} h\omega_1 \vec{v}_1$ where n_1/V is the number of phonons per unit volume in mode 1. For a three phonon process

$$\Delta\vec{J} = \frac{\hbar}{V} [\omega_2\vec{v}_2 + \omega_3\vec{v}_3 - \omega_1\vec{v}_1] \tag{33}$$

will be the change in the heat current. For Debye phonons

$$\vec{v} = \omega\vec{q}/|q|^2 \tag{34}$$

so

$$\Delta\vec{J} = \frac{\hbar}{V} [\frac{\omega_2^2}{|q_2|^2} \vec{q}_2 + \frac{\omega_3^2}{|q_3|^2} \vec{q}_3 - \frac{\omega_1^2}{|q_1|^2} \vec{q}_1] \tag{35}$$

$$= \frac{\hbar}{V} v^2 [\vec{q}_2 + \vec{q}_3 - \vec{q}_1] \tag{36}$$

But for Normal processes

$$\vec{q}_1 = \vec{q}_2 + \vec{q}_3 \tag{37}$$

Hence $\Delta J = 0$ for Normal processes. Note also that this argument breaks down when there is dispersion. Thus, processes which conserve wave vector cannot affect the rate at which a system comes to equilibrium in a direct manner. Normal processes also are called N-processes. Processes for which $G \neq 0$ are termed Umklapp (German for "flipping-over") processes, and from the previous argument one can see if $\omega'' = \omega + \omega'$ and $\vec{q}'' - \vec{q}' - \vec{q} = \vec{G} \neq 0$ then one does indeed obtain a rate of change for N_q. Due to the fact that the designation of certain processes as Umklapp or Normal depends upon the choice of Brillouin Zone structure; it may seem that this designation is arbitrary, but, in fact, once the choice is made the distinction is also made, and no difference of results follow.

The statement that Normal, unlike Umklapp, processes can have no direct effect on the thermal heat flow does not mean they have no effect at all. Since N-processes generate intermode repopulation, phonons with long mean free paths may be channeled into (q,p) states which are more subject to scattering and vice versa. Thus N-processes have an indirect effect on the thermal conductivity which, in many cases, cannot be ignored. Because of the intermode repopulation changes, the phonon distribution responds in a different way from the change produced by static impurities, and the relaxation time approximation must be used with care. The usual way to determine an effective relaxation time for The case where several scattering processes simultaneously is to use Matthiessen's rule [22] as discussed earlier, when each scattering process can be characterized by relaxation time,

$$\tau^{-1} = \Sigma_i \tau_i^{-1} \tag{38}$$

This approximation, however, cannot be used in the case where Normal processes must be considered as in the case of very pure anharmonic crystals (for example ^{4}He) or in the case where static processes alone cannot account for the form of the experimental conductivity curve [23]. The reason is because a relaxation time for a Normal process can refer not to a spatial flux of energy, but only with the rate at which energy is transferred locally from one mode to another of the phonon system [21].

The model most generally referred to in the literature to account for N-processes as well as U-processes and other directly resistive mechanisms is Callaway's [24] modification of the Debye formulation given in Equation (26) He considered that the N-processes restored a

phonon distribution not to equilibrium (Eq. (20)) but to the "displaced" or drifting distribution, Equation (39). The directly resistive processes are considered to restore any nonequilibrium distribution to the distribution of Eq. (20) and the total rate of change of the distribution is given by

$$\frac{\partial N_q}{\partial t} = -\frac{N_q - N_q^o}{\tau R} - \frac{N_q - N_q(\vec{u})}{\tau R} \tag{39}$$

where $N_q(u)$ is given by Eq. (39). Upon assuming a Debye model and writing $1/\tau_c = 1/\tau_R + 1/\tau_N$ his expression for the thermal conductivity can be written

$$\lambda = \lambda_1 + \lambda_2 \tag{40}$$

$$\lambda_1 = \frac{k}{2\pi^2 v}\left(\frac{k}{\hbar}\right)^3 T^3 \int_0^{\Theta_D} \frac{\tau_c x^4 e^4}{(e^x-1)^2}\, dx \tag{41}$$

$$\lambda_2 = \frac{k}{2\pi^2 v}\left(\frac{k}{\hbar}\right)^3 T^3 \frac{\left\{\int_0^{\Theta_T} (\tau_c/\tau_N) x^4 e^x (e^x-1)^{-2} dx\right\}^2}{\int_0^{\Theta_T} (\tau_c/\tau_N \tau_R) x^4 e^x (e^x-1)^{-2} dx} \tag{42}$$

The conductivity λ_1 treats N-processes on the same footing as resistive processes and consequently underestimates it. This loss is presumably made up through the addition of a conductivity λ_2, Equation (42).

In reality, though, most experimental results are treated with resistive processes dominant, τ_R being frequency dependent, so further progress requires a discussion of the nature of the specific processes reflected by the relaxation times used to determine τ_R. Table II summarizes the frequency and temperature dependence of relaxation times

TABLE II

COMMONLY EMPLOYED RELAXATION TIME EXPRESSIONS

	τ^{-1}
Boundary scattering	v/LF
Point defect	$A\omega^4 \qquad A = (V\Gamma/4\pi v^3)$
Phonon-phonon	$\Gamma = \Sigma_i f_i (\frac{\Delta Mi}{M})^2$
Normal	$B_1\omega^2T^3$
Umklapp	$B_2\omega^2T^3e^{-\Theta/\alpha T}$
	$B_2\omega^2Te^{-\Theta/\alpha T}$ high temperature
Dislocation	$D\omega$
Resonant scattering	$\frac{R\omega^2T^P}{(\omega_o^2 - \omega^2) + (\Omega/\pi)\omega^2\omega_o^2}$

v is an average phonon velocity, L is the radius of the sample, F is the structure factor for non-circular cylinders, $V = a_o^3$ = the molecular volume, f_i is the defect concentration, ΔMi is the mass defect difference from the molecular mass M, and Ω is a damping factor.

commonly employed. The parameters A, B_1, C, D, etc. are adjusted to give the best fit to the data for low temperatures. For high temperatures ($T > \Theta_D$) $\tau^{-1} = B_2 \omega^n T^m \exp(-\Theta_D/\alpha T)$ where B_2 and α are adjusted to fit the data for Umklapp processes.

CHAPTER II

PHONON SPECTROSCOPY AND THERMAL CONDUCTIVITY

Experimental thermal conductivity curves may be modeled fairly accurately for most crystalline insulating solids by using Equation (41) alone. Relaxation times for specific scattering mechanisms are, as shown in Table II, functions of both frequency and temperature in general and are combined according to Eq. (38). In practice the constants are adjustable parameters which are varied to give the best fit, and their values reflect the strengths of the particular processes. If the analysis consisted of no more than this, it would be of uncertain value to the understanding of the physics of phonon processes. Theoretical calculations of the relaxation times for specific processes indicate, to some extent, how these parameters are related to other properties of the material being studied. These put ranges on the values that correspond to known facts; and these calculations indicate how the strengths ought to vary with properties such as density, structure, sound velocities, etc. The end result of this procedure of fitting and comparing is a set of scattering rates for thermal phonons for a particular sample. But one can see from inspecting the thermal conductivity integration that the relaxation times extracted are independent of phonon dispersion, polarization, direction; and, in addition, only a weak structural dependence seeps in through the group velocity averaging and the Debye temperature.

A more satisfactory picture of phonon interactions would be given if one could obtain from an experiment, knowing the crystal structure and force constants to all relevant orders, the probability of a phonon of (group) velocity $\vec{v}$, and wave vector $\vec{q}$ propagating in the (a,b,c) direction, colliding with another phonon of velocity $\vec{v}$, wavevector $\vec{q}'$ propagating in the direction (a',b',c'), and producing a third phonon of $(\vec{v}'',\vec{q}'')$ moving in the (a'',b'',c'') direction, or vice versa. Such an experiment would require monitoring the temporal, spatial, and spectral evolution of a sharply characterized phonon distribution, preferably "monochromatic" in energy and having known polarization. Although no such experiments exist which satisfy all the features of the ideal experiment, recent developments in nonequilibrium phonon studies have shown that some of the problems can be addressed, and in particular, something can be known of the lifetimes of phonon against anharmonic decay.

Heat Pulses and Optical Techniques

A general review of recent developments in phonon spectroscopy has been given by Bron [20] and only those methods of interest to this study will be touched on here.

Until 1964, only thermal conductivity measurements, combined with a Debye-type analysis, could yield experimental information on the scattering properties of phonons in the terahertz region. In 1964 von Gutfeld and Nethercot [25] introduced a heat pulse technique whereby they produced nonequilibrium short-duration heat pulses which were shown to propagate "ballistically" through a crystalline sample at low temperatures. Their time-of-flight method of detection reveals pulse struc-

ture at the detecting bolometer as a function of time and could be seen to result from the separation of the phonon distribution with time into longitudinal and transverse distributions, which because of the differing group velocities had differing arrival times at the bolometer. The "temperature" of the heat pulses was a measure of the frequency of the dominant phonons. Heat pulses alone have been used to study the interaction of phonons with impurities by comparing the ratio of longitudinal to transverse signal arrival strengths between the doped and the undoped samples. But heat pulses in combination with optical excitation and detection moves the phonon phenomena to the much more experimentally accessible visible region of the electromagnetic spectrum.

The first true phonon spectrometer was the spin-phonon spectrometer described and demonstrated by Anderson and Sabisky [26]. A vibronic sideband phonon spectrometer was demonstrated by Bron and Keilmann [27] and Bron and Grill [28]. They used the vibronic sidebands of Eu^{3+} in SrF_2 to study the spatial, temporal, and spectral evolution of various phonon distributions introduced as heat pulses. By monitoring the luminescence of the $4f^6 5d - 4f^7$ transition as a function of heater power, (and thus dominant phonon energy) they were able to demonstrate that higher frequency phonons decay more rapidly than low frequency ones as expected but they could not confirm the prediction of Orbach and Vredevoe [29] and Klemens [30], that $\tau^{-1} = A\omega^5$, where

$$A = \frac{\hbar[(C_1+C_4) + \frac{3}{2}(C_2+C_5)]^2}{16\pi\rho^3 V_l^6 V_t^3} \left(1-\frac{V_t^2}{V_l^2}\right) \left(\frac{V_t^2}{V_l^2} - \frac{V_t}{V_l} + \frac{3}{8}\right) \text{ (Orbach)} \qquad (43)$$

or

$$A = (3\pi/f\sqrt{2})\gamma^2\left(\frac{\hbar}{Mv^2}\right) \frac{V_l \hbar}{V_t k_3^3 \theta_D^3} \text{ (Klemens)} \qquad (44)$$

where C_i is a third order elastic constant, ρ is the mass density, V_l, V_t are the longitudinal and transverse phonon group velocities, M is the unit cell mass, γ is the Grüneisen parameter, V the sound velocity, and Θ_D is the Debye temperature.

Later measurements by Baumgartner et al. [31], using a variation of the vibronic sideband spectrometer which employed stress split states of Eu^{3+} in CaF_2 to monitor the phonon frequencies more precisely, did show that the scattering rate of terahertz phonons varied as ω^5. They found $\tau^{-1} = 5.6 \times 10^{-60}\omega^5$. (See Fig. 6).

More recently Will et al. [13] used a spin-phonon spectrometer with $LaF_3:Er^{3+}$ where the $^4S_{3/2}$ (1) level was split and varied with an external magnetic field. They obtained an anharmonic decay rate of $\tau^{-1} = 4.2 \times 10^{-58}\omega^5$ for teraherz phonons, as shown in Figure 7.

Although earlier works had monitored phonon lifetimes, they were limited to lifetime measurements for specific phonon frequencies, such as $29cm^{-1}$ (0.87THz) phonons in ruby. Table III summarizes some results of these previous studies.

Relation to Thermal Conductivity

The experiments with heat pulses and those of steady thermal transport both deal with nonequilibrium phonon distributions, but there is a fundamental difference, other than the temporal one, between these. In heat pulse experiments the phonons injected by a heater or a laser or whatever, are at a much higher temperature than the thermal bath. When the higher frequency phonons decay, they generally split into two phonons of comparable energy and these phonons split likewise until the energy is distributed to the thermal bath at low temperature. The

TABLE III

LIFETIMES FOR SPECIFIC PHONONS IN VARIOUS MATERIALS

from Bron [32]

ν (THz)	Crystal	Method	τ_ℓ(Exp.) (sec)	τ_ℓ(Theor.) (sec)
0.69	$LaF_3:Pr^{3+}$	RPS	$1.5X10^{-8}$	$6.0X10^{-7}$
0.87	$Al_2O_3:C^{3+}$	RPS	$4.0X10^{-8}$	$4.6X10^{-6}$
1	$SrF_2:Eu^{2+}$	VSPS	$3.0X10^{-7}$	$2.5X10^{-8}$
2	$SrF_2:Er^{2+}$	VSPS	$2.5X10^{-7}$	$2.1X10^{-9}$
3	$SrF_2:Eu^{2+}$	VSPS	$2.0X10^{-7}$	$2.7X10^{-10}$
3.4	SiO_2	CPG	$> 4.0X10^{-7}$	$2.3X10^{-10}$
3.5	$CaF_2:Sm^{2+}$	RPS	$> 4.0X10^{-8}$	$3.3X10^{-10}$

RPS: Ruby Phonon Spectrometer

VSPS: Vibronic Sideband Phonon Spectrometer

CPG: Coherent Phonon Generation

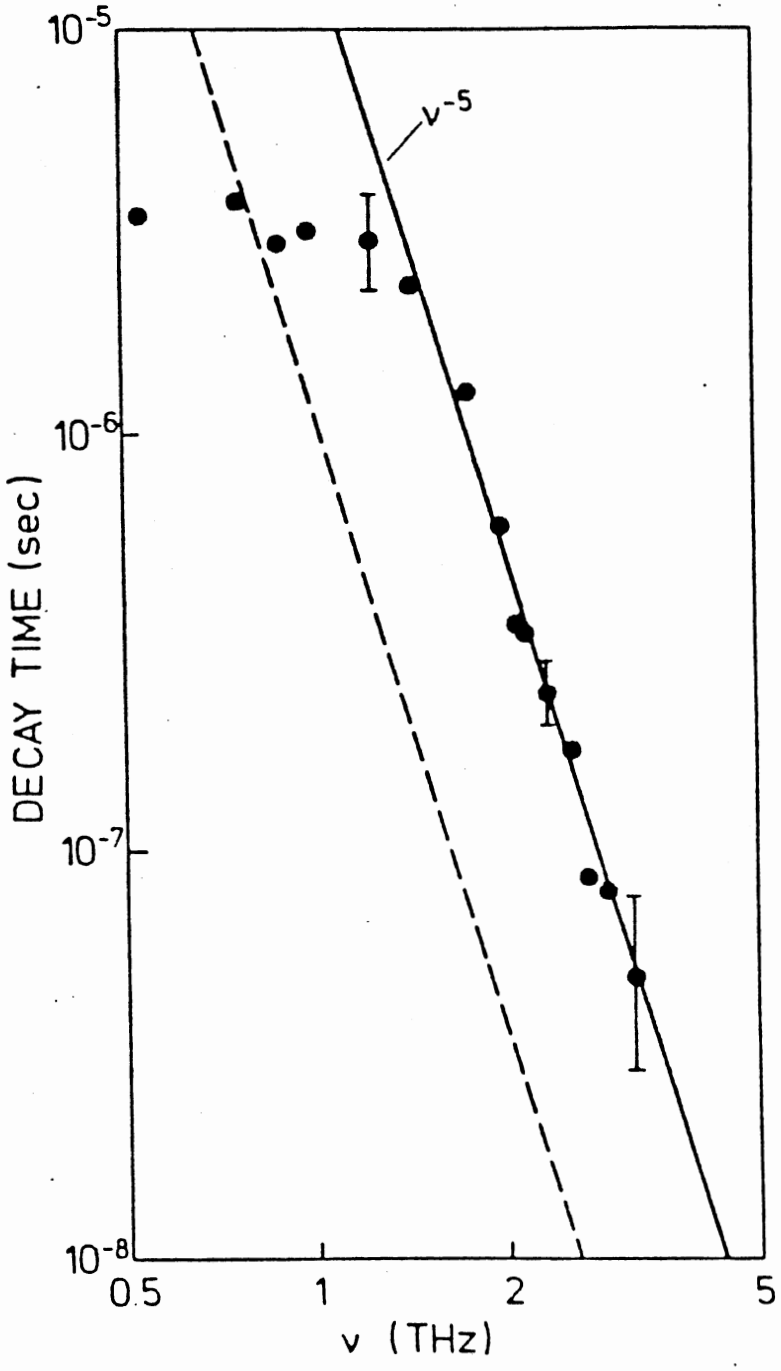

Source: 31

Figure 6. Lifetimes of Acoustic Phonons in CaF_2

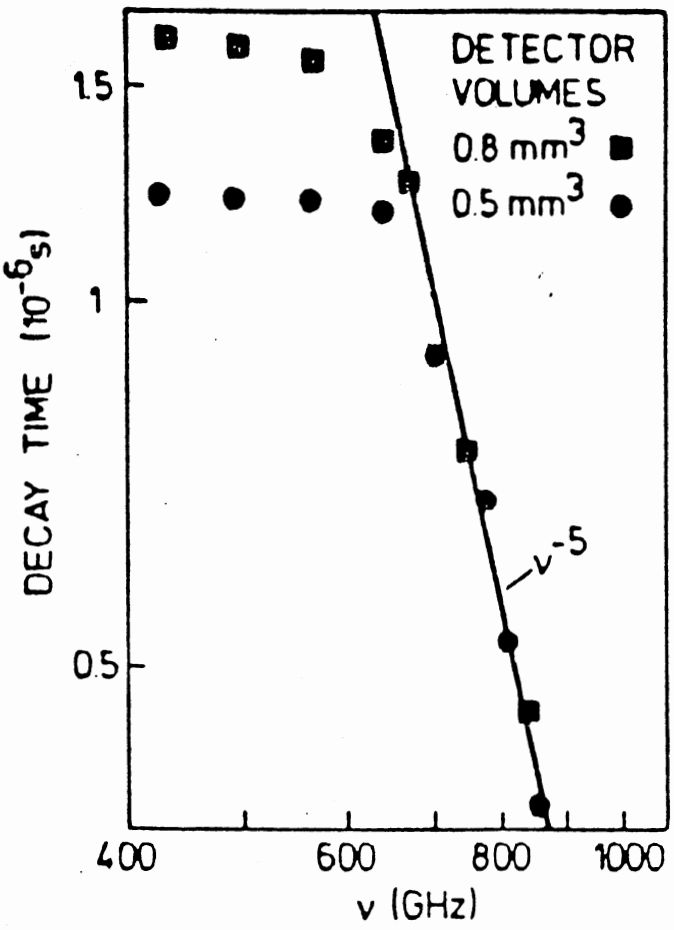

Source: 13

Figure 7. Lifetimes of Acoustic Phonons in LaF_3

reason for this is that there are no higher ω phonons present for the injected distribution to interact with and so they simply decay away.

On the other hand, in thermal conductivity, the injected phonons are not far from equilibrium, and the distribution interacts with the indigenous thermal phonon population. Any comparison of the results of monochromatic experiments to thermal experiments must take this into account. In general, accounting for this is difficult but the following simplified analysis may shed some light on this point. Assume that in the absence of thermal phonons $\tau = C\omega^5$ and, for Case I, Fig. 8,

$$\frac{\partial \Xi(\omega)}{\partial t} = -C\omega^5 \delta\Xi(\omega), \quad \Xi(\omega) = g(\omega)N(\omega) \tag{45}$$

$N(\omega)$ is the phonon occupation number, $g(\omega)$ is the phonon density of states, and their product, $\Xi(\omega)$, is the phonon population. Now we expect the interactions having the diagrams in Case II in Fig. 8 to have the highest probability of occurrence. For example, for the upper interactions of Case II,

$$\frac{\partial \Xi(\omega)}{\partial t} = -C\omega^5 \{\Xi(\omega)[\Xi(\omega/2) + 1]^2 - [\Xi(\omega) + 1]\Xi^2(\omega/2)\} \tag{46}$$

and let $\Xi(\omega/2) = \Xi_o(\omega/2)$, $\Xi(\omega) = \Xi_o(\omega) + \delta\Xi$ where Ξ_o is the equilibrium (Bose) population function and $\delta\Xi$ is the deviation,

$$\frac{\partial \Xi(\omega)}{\partial t} = -C\omega^5 \{[2\Xi_o(\omega/2) + 1]\delta\Xi - \Xi_o^2(\omega/2)\} \tag{47}$$

Ignoring $\Xi_o^2(\omega/2)$ we get

$$\frac{\partial \Xi(\omega)}{\partial t} = -C\omega^5[2\Xi_o(\omega/2) + 1] = [-\frac{4k}{\hbar} C\omega^4 T - C\omega^5]\delta\Xi \tag{48}$$

where

$$C\omega^5 << (4k/\hbar)C\omega^4 T \tag{49}$$

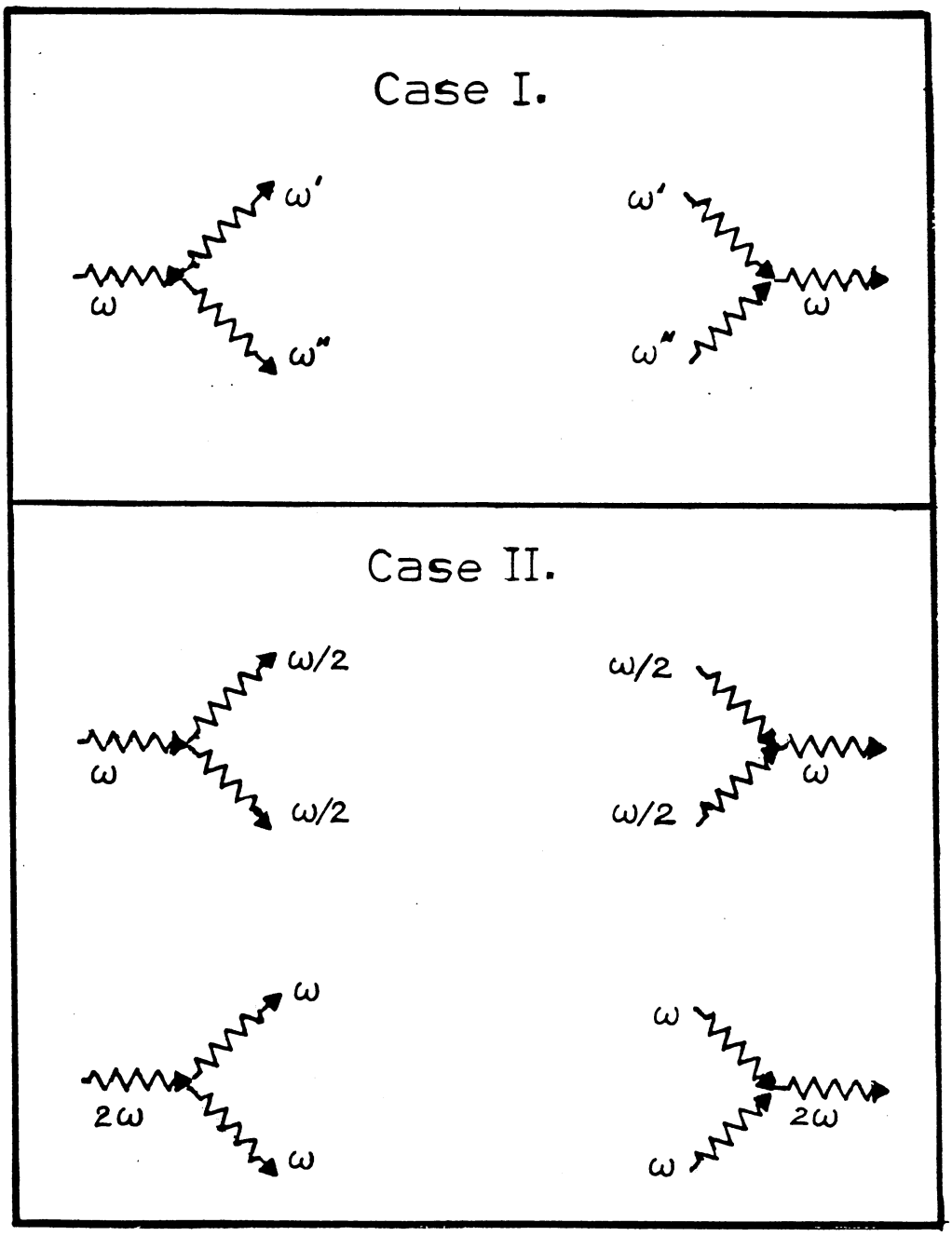

Figure 8. Phonon Interactions

For the lower interactions of Case II, we employ the principle of detailed balance

$$\frac{\partial \Xi(\omega)}{\partial t} = -2 \frac{\partial \Xi(2\omega)}{\partial t} \tag{50}$$

$$= 2C(2\omega)^5 \{\Xi(2\omega)[\Xi(\omega + 1]^2 - [\Xi(2\omega) + 1]\Xi^2(\omega)\} \tag{51}$$

$$= 64C\omega^5 \{\Xi_o(2\omega)[\Xi_o(\omega)+\delta\Xi+1]^2 - (\Xi_o(2\omega)+1)(\Xi_o(\omega)^2+2\Xi_o\delta\Xi+\delta\Xi^2\} \tag{52}$$

$$= -64C\omega^4 T\delta\Xi(\frac{k}{\hbar}) \tag{53}$$

where

$$\Xi_o(2\omega) = (e^{2\hbar\omega/kT}-1)^{-1} \sim (2\hbar\omega/kT)^{-1} \tag{54}$$

Thus, adding Eq. (48) to Eq. (53), gives

$$\frac{\partial \Xi(\omega)}{\partial t} = -68C\omega^4 T(\frac{k}{\hbar})\delta\Xi = -\frac{\delta\Xi}{\tau} \tag{55}$$

and $\tau^{-1} = C'\omega^4 T$ for anharmonic decay in the thermal environment. We propose, then, to model the phonon-phonon portion of the thermal conductivity term with this form rather than the more or less phenomenological $\omega^2 T$ and $\omega^2 T^3$ terms extensively employed in the literature. The relation between the constants for the thermal experiment and the anharmonic decay experiment is

$$C' = C_{thermal} = 68(\frac{k}{\hbar})\ C_{monochromatic} = 68(\frac{k}{\hbar})C \tag{56}$$

$$C' = 8.91 \times 10^{12}\ C \tag{57}$$

Practically, we propose to fit the thermal conductivity curve with the C_{th} parameter and compare with the results of the monochromatic experiment.

In summary, the purposes of this study are to measure the thermal conductivities of LaF_3:0.1%Er^{3+} in two directions, and of CaF_2; to model the results with a Debye integral to determine what scattering mechanisms are dominant; and finally, to compare the estimated scattering strengths obtained from theory and other experiments with those obtained here.

CHAPTER III

EXPERIMENTAL PROCEDURE

Sample Preparation

The LaF_3 samples were cut from a single crystal boule (3 cm X 1 cm dram) grown by the Stockbarger method, and were provided by Optovac. The c-axis of the crystal was known to be oriented at about 70° to the boule axis. A wafer sawed from the boule had the corners cut, and edges were polished all around. The c-axis was then located by observing the crystal between crossed polarizers. From a wafer 3 mm thick a parallelepiped 2.87 X 3.00 X 6 mm was prepared for the c-axis ($\lambda_{||}$) sample. The ends were lightly roughened with 600 grit silicon carbide powder. Although the length was somewhat shorter than would be desired, it was still useable.

Two samples whose long dimensions were perpendicular to the c-axis ($\lambda_{\perp}$ samples) were prepared, having dimensions 3.1 X 2.84 X 14 mm. The sides were left as they came from the diamond saw. Aluminum blocks (6 mm in length) having approximately the sample cross section were epoxied to one end of the $\lambda_{\perp}$ sample. This was done since the crystal tended to crack when clamped directly to the holder. A copper spool clamped to the opposite end provided for winding the gradient heater coil. No other treatment of the sample other than cleaning with ethyl acetate was performed.

Experimental Procedure

Description of The Apparatus

The transport of heat through an isotropic solid is described macroscopically by

$$J = -\lambda \vec{\nabla} T$$

where J is the power flux per unit area. For one dimensional steady state transport

$$J = \frac{P}{A} = -\lambda \frac{dT}{dx}.$$

If the power input from the high temperature end is constant in time then the temperature gradient is linear in x (and negative in sign) and

$$\lambda = \frac{P}{\Delta T} \left(\frac{\ell}{A}\right)$$

where $(\frac{\ell}{A})$ is a measure of the geometry of the heat flow region between the temperature sensors. Typical values range from ~4 cm^{-1} for stubby samples to ~50 cm^{-1} for slender samples. Basically the experiment consists of introducing a known amount of heat energy into one end of the sample to produce a temperature gradient which is reflected as a temperature difference between the two sensors. The heat energy introduced is small enough that the temperature difference between the thermometers is much less than the absolute temperature of the sample, yet large enough to easily measure. Generally, $\Delta T \sim 0.05T$.

The experimental arrangement used in this study is shown in Figure 9. The thermometers were made up from gold wire alloyed with .07% iron, and copper. In the arrangement shown three signal wires were brought out of the cryostat. A thermocouple made with the gold wire was immersed in an ice bath and served as the reference junction for the ambient temperature voltage which was read from a Hewlett-Packard

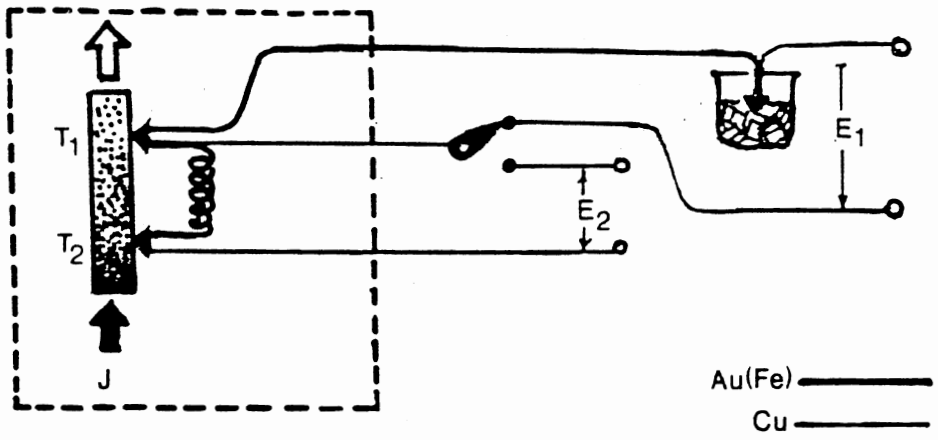

Figure 9. Schematic of the Experiment

digital voltmeter. The other two wires of copper carried the differential EMF produced between the thermocouples made up with a gold alloy jumper. This voltage was measured with a Honeywell Model 2779 microvolt potentiometer in combination with a Leeds and Northrup Model 9838 Guarded Nanovolt Galvanometer. The arrangement allowed EMF readings to the nearest hundredth of a microvolt. The gradient heater consisted of about 30Ω of constantan wire wrapped onto a small metallic spool. The voltages and currents of this heater were read with a digital voltmeter.

The sample mounting geometry is illustrated in Figure 10. The thermocouples were attached to copper clamps with indium solder and the clamp contact surfaces were faced with indium metal to increase the thermal contact. The heater spool described earlier was mechanically clamped to the end of the $\lambda_{\perp}$ sample.

The samples were initially physically and thermally attached to the heat sink (cold finger) of the cryostat through a clamping block of aluminum or copper epoxied to the end of the sample. It was later found that this arrangement produced poor thermal contact between the sample and the heat sink, and so it was dropped in favor of mechanically clamping the sample directly to the heat sink.

The $\lambda_{||}$ sample was so short (ℓ = 6 mm) with respect to its cross section (3 mm X 3 mm) that the method of mounting the heater and attaching the sample itself to the heat sink as was done with the λ sample would not work.

A special holder, illustrated in Figure 11, was designed and was found to function well in practice. The sample, whose ends were reasonably flat and parallel were sandwiched between the heat sink, contact, and the heater, "A", where each acted as the face of a spring loaded

a - cold finger
b - constantan heater
c - sample mounting clamp
h - clamping block
d,f - thermocouple clamps
e - gold/iron jumper
g - gradient heater
k - sample

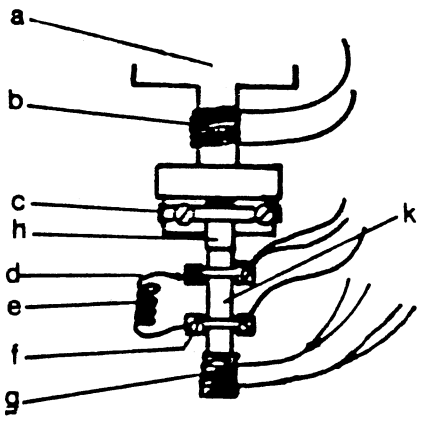

Figure 10. Physical Arrangement for the $\lambda_{\perp}$ Sample

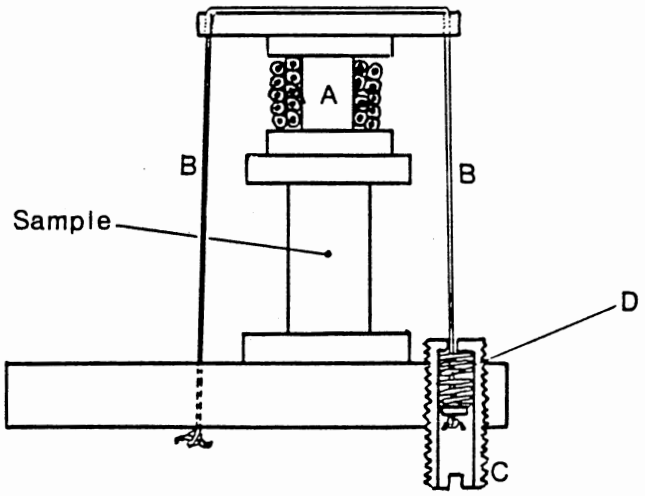

Figure 11. Physical Arrangement for the λ_{II} Sample

clamp. The tension in the nylon filament, "B", was adjusted by turning the screw "C", while the spring, "D", maintained tension in the presence of thermal expansion of the sample or holder. The contact surfaces were faced with indium and scraped flat.

In Fig. 12, the sample shown at "t" along with its attachments were mounted in the evaculated chamber "r" of the cryostat shown in cross-section. The cryostat itself consisted of three main parts; the glass dewars "h" and "m", the sample chamber, and the conduit tubes which also supported the chamber.

The concentric Pyrex dewars thermally isolated the sample chamber and contained the cryogenic fluids used. Liquid nitrogen was introduced into the space "l" between the inner wall of "h" and the outer wall of "m". Liquid He^4 was introduced into the inner dewar. The chamber itself consisted of a stainless steel flange to which was bolted a demountable flanged stainless cylinder "s". Indium wire was used as a leak proof gasket. Conduit "v", also stainless, served to connect the chamber with the pumping systems, and to pass signal and control wiring from the sample to the feedthrough and out to the instrumentation. Conduit "v", connected the copper helium pot "p" with its vacuum system, through valve "y". A smaller tube connected the coldfinger "q" with a helium gas source through valve "z", and was protected by a popoff valve "b". The cold finger itself consisted of a copper rod, "u", internal to and concentric with a stainless tube "o". The interspace between "u" and "o" thermally coupled the cold finger to the helium bath, and this coupling depended on the amount of exchange gas present, and was adjusted during the course of the experiment. Copper heat shield flanges "f" soldered to the tubing also added strength to the assembly. A needle

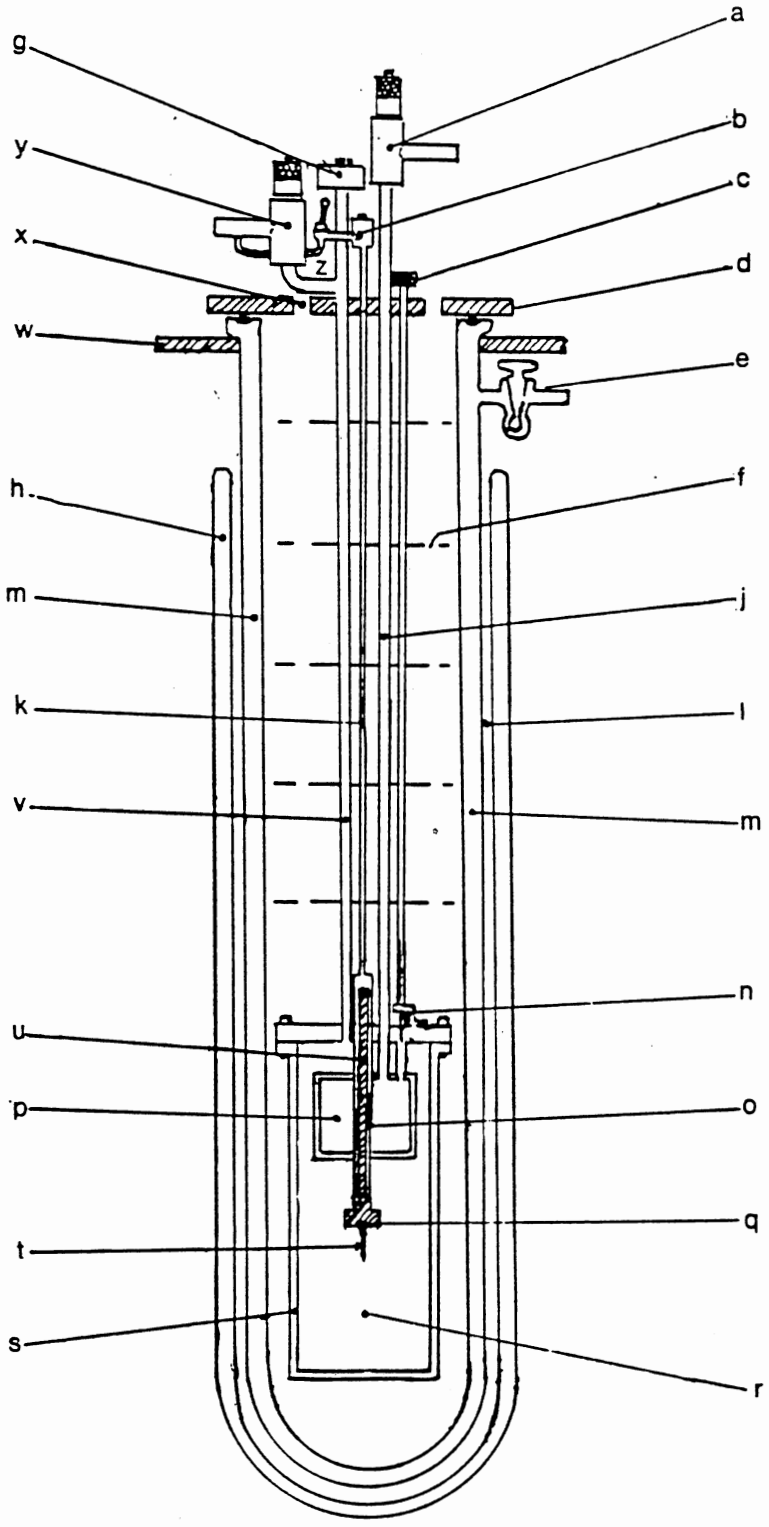

Figure 12. Diagram of the Cryostat

valve "n" was operated through a hollow shaft terminated by knob "c". The orifice of the valve allowed helium liquid surrounding the chamber into the pot. This quantity of helium was pumped thrugh tube "j" and valve "a" to lower the vapor pressure and thus the temperature of the helium. The lowest temperature limit of the present system was about 1.5 K and varied from run to run. The length of the cryostat overall was about one meter and the internal assembly could be easily removed and handled by one person. The tube assembly passed through a stainless flange "d" which rested upon an o-ring in a groove on the top of the inner dewar. These were clamped during the course of the experiment. The sample chamber was thus suspended from the flange via the conduit tubes, the flange was supported by the inner dewar which was, in turn, supported from its own lip by ring "w", a part of the support frame (not shown). The outer dewar "h" was supported separately at its bottom. Spacers keep the dewars from physical contact. The inner dewar "m" was evacuated anew between runs, through stopcock "e".

All signal and control wiring was wrapped several turns about the cold finger post to help prevent thermal gradients from adding nonsystematic EMF's to the thermal EMF's.

The first step in conducting an experiment was to check all wiring connections before sealing the chamber. After the chamber was bolted together, it was pumped out and the vacuum was checked using a modified commercial helium leak detector. If the vacuum was satisfactory the assembly was placed in the dewar set and all vacuum and electrical connections were made. After the electrical connections were all tested, all chambers of the cryostat were pumped out and usually left for about 24 hours at room temperature during pump down.

The cool down was accomplished in two stages. After helium gas was introduced into chamber "r" and the exchange gas chamber "u"-"o", liquid nitrogen was poured into the inner dewar. After about one hour the sample was generally within a few degrees of 77.4 K. The helium exchange gas in "r" was then pumped out and a reading of ΔT was taken and λ was calculated. If this value was close to being correct, the precooling liquid nitrogen was pumped from the dewar through opening "x" to the space between the dewars through a plumbing arrangement not shown in Figure 11. ^{4}He exchange gas was reintroduced into chamber "r" and the second stage of cool down, the helium transfer, proceeded. Liquid helium then filled the inner dewar to a depth of about 15 cm above the surface of the sample chamber. After the liquid was introduced into the pot "p", it was pumped to the lowest temperature possible and reading began.

The reading procedure was to note the ambient temperature and take a reading of the baseline EMF between the thermometer while under (near) thermal equilibrium. Then the heater current was turned on and set to a value between 1 mA to 20 mA. The resulting temperature gradient was reflected as a deflection in the potentiometer galvanometer. Once steady state conditions were reached, the galvonometer was rebalanced, and the gradient EMF was recorded. The heater was then shut off and the ambient temperature and baseline gradient were noted (but not recorded). If drift during the time of heating was negligible, λ was calculated and plotted. This was repeated for higher heater powers. The ambient temperature was controlled by adjusting the ambient heater, the exchange gas, the pumping rate, and the amount of helium remaining in the pot. The cryostat performed satisfactorily in the temperature range between

1.8 K to 100 K. At the lowest temperature, measurements may be taken about as quickly as the controls can be operated, because the heat capacity of the system is small, but as the temperature rises, longer equilibration times occur and measurements may take several minutes.

Thermometry

For both the LaF_3 and the CaF_2 samples the ambient and gradient temperatures were measured with copper wire versus gold wire alloyed with 0.07% iron. The tables used to convert the thermal EMF to temperatures for this thermocouple were published by Sparks & Powell, J. Res. Nat'l Bureau of Standards 76A, 263 (1972). It was shortly found that the thermocouples made with the wires available demonstrated a systematic variation from the NBS Tables. This is not surprising since the thermopower of the thermocouple is strongly dependent upon the concentration of the magnetic iron atoms in the gold component, which can vary from spool to spool. Comparing their tables with the readings from the Honeywell potentiometer, our thermocouple read "75.1 K" for liquid nitrogen immersion and "2.73 K" for liquid helium immersion. This required a correction to the table temperatures where the actual temperature was given approximately by

$$T_1 = (1.00822)T' + 1.44 \qquad (58)$$

where T' was the temperature from the tables. The normal boiling points of ^4He and N_2 were used as fixed points to determine their correction. This temperature correction was used for the measurements of the $\lambda_\perp$ sample of $LaF_3:Er^{3+}$.

Due to experimental changes prior to the measurements on the $\lambda_{||}$

sample and the CaF_2 sample another set of thermocouples were made, and these were found to vary from the T_1 values by an additional +0.08K throughout the temperature range of interest. Thus,

$$T_2 = (1.00822)T'+2.01. \tag{59}$$

New tables of T_1 were made up and used for all the measurements. The dE/dT were not affected and were used as dE/dT_0 for E_1 and dE_2/dT_0 for E_2 as well, where E_1 and E_2 were the thermal EMF's of the two sets of thermometers, as the E vs. T curves were basically just shifted rigidly along the temperature axis.

Sources and Estimation of Errors

From experience, the errors in thermal conductivity measurements are expected to limit the absolute accuracy to around 15% or so. The origin of these errors come from several sources. Probably the largest contribution comes from geometrical and thermal contact considerations. The next largest source of errors is most likely from heat losses which largely affect the gradient temperature readings. Another source of error lies within the calibration of the voltmeters and potentiometer.

Geometrical and Thermal Contact Errors

The thermal conductivity can be written

$$\lambda = \frac{IV\ell}{A\Delta T} \tag{60}$$

where ℓ is the average thermometer clamp separation, ΔT is the temperature gradient, IV is the heat power and A the cross-sectional area. If dimensional errors were the only ones considered then

$$\Delta\lambda = \frac{IV\Delta\ell}{A\Delta T} + \frac{IV\ell}{\Delta T}\left(-\frac{\Delta A}{A^2}\right) = \frac{IV}{A\Delta T}\left(\Delta\ell - \frac{\ell\Delta A}{A}\right). \tag{61}$$

If $A = d_1 d_2$, $\Delta A = d_1(\Delta d_2) + d_2(\Delta d_1)$

Then $$\frac{\Delta\lambda}{\lambda} = \frac{\Delta\ell}{\ell} - \frac{\Delta A}{A}. \tag{62}$$

The dimensions of the samples, the thermometer clamp separations, and the percent errors are given in Table IV. The uncertainties in the table for the d_i come from a measurement error of the vernier caliper of 0.001" (~0.0025cm). The uncertainty in ℓ comes from the finite width of the thermocouple contact faces and represent the uncertainty in the effective thermocouple positions. If the thermal contact between the thermocouple and the sample was bad, one would expect the separation of the thermocouples to be represented by the distance between the points of best contact with the clamps. If the thermal contact was good, the distance between the thermocouples then would be represented by the separation of their centers. Since each thermocouple has a width of ~1mm, this value gives the uncertainty. Most likely, the thermal contact remained unchanged throughout a measurement series, and the actual geometric errors are smaller than those of the table.

Heat Loss Errors

Heat escapes through signal and control wires, poor vacuum, radiation, and desorption. The two largest potential sources of error from the conduction of heat through wires would be through thermal conduction of part of the heater power down along the contstantan wires making the heater connection; and thermal shorting across the gold jumpers (See Fig. 9). If these affect the heater power and the temperature gradient, then, if $P = IV$ is the heater power,

TABLE IV

GEOMETRIC ERRORS

	d_1 (cm)	d_2 (cm)	Δd (cm)	A (cm^2)	ΔA (cm^2)	ℓ (cm)	$\Delta\ell$ (cm)	$\Delta\lambda/\lambda$ (%)
λ	0.284	0.310	0.003	0.0880	0.002	0.753	0.10	11.0
λ	0.295	0.295	0.083	0.0870	0.002	0.290	0.10	32.2
λ_{CaF_2}	0.305	0.297	0.003	0.0906	0.002	1.580	0.10	4.12

$$\delta\lambda = \frac{\delta(IV)\ell}{A\Delta T} - \frac{IV\ell\delta(\Delta T)}{A(\Delta T)^2} = \frac{\ell}{A\Delta T}\left(\delta P - \frac{P\delta(\Delta T)}{\Delta T}\right) \tag{63}$$

and $$\frac{\delta\lambda}{\lambda} = \frac{\delta P}{P} - \frac{\delta(\Delta T)}{\Delta T} \tag{64}$$

The last expression states that both errors represent reductions. From calculation in Appendix A is shown that $\delta P/P \sim 1\%$ and $\frac{\delta(\Delta T)}{\Delta T} \sim 0.1\%$ at worst. Thus, heat loss through conduction $\frac{\delta\lambda}{\lambda}$ is practically swamped by the geometric errors.

For imperfect vacuum, the heat loss calculation is somewhat ambiguous because of the presence of desorption. If desorption phonomena are ignored, a theoretical estimate for residual gas is calculated in Appendix B to be $\sim 3\mu\omega$.

The radiation losses are calculated in Appendix C and must be taken into account for measurements at temperatures above 80K.

CHAPTER IV

RESULTS AND ANALYSIS

The results of the LaF_3 thermal conductivity measurements are shown in Figures 13 and 14, and the CaF_2 data is plotted in Fig. 15. The $\lambda_{||}$ and $\lambda_{\perp}$ of the LaF_3 peak at about 14 K and show similar behavior with temperature except for the absolute magnitudes. Both samples have nearly the same thermal conductivity at 2 K and the two curves gradually diverge from thereon. As expected, the c-axis sample has a larger thermal conductivity in the peak region. Both $\lambda_{||}$ and $\lambda_{\perp}$ fall slower than the theoretically expected T^3 at low temperatures. The λ curve exhibits $\lambda_{\perp} \sim T^{\alpha}$, $\alpha = 2.16$, while $\lambda_{||}$ shows $\alpha = 2.62$.

The CaF_2 thermal conductivity showed scatter in the peak region but the points at low temperature lie fairly close to $\alpha = 3.08$ which is quite close to the value expected for Casimir scattering. The curve obtained in this study is similar in both magnitude and shape to those for similar undoped samples in the literature [15] [16] [17]. Thermal conductivity data for all samples are tabulated in Appendices E, F, and G.

Theoretical Estimates of Scattering Strengths

The nature of phonon scattering in crystals has already been touched on in the first two chapters. In this chapter, the relaxation times used to fit the experimental curves are presented and discussed.

To begin with, it would be useful to estimate the Grüneisen anhar-

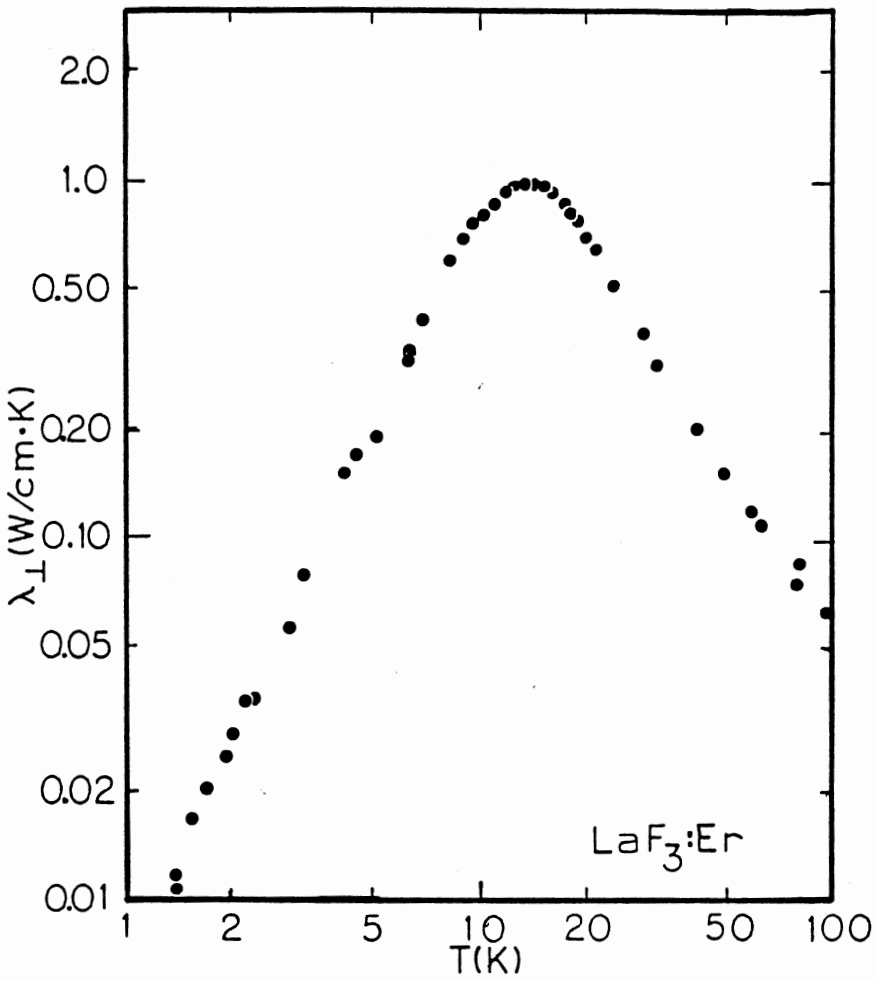

Figure 13. Thermal Conductivity of LaF_3:0.1%Er^{3+} Perpendicular to the C-axis

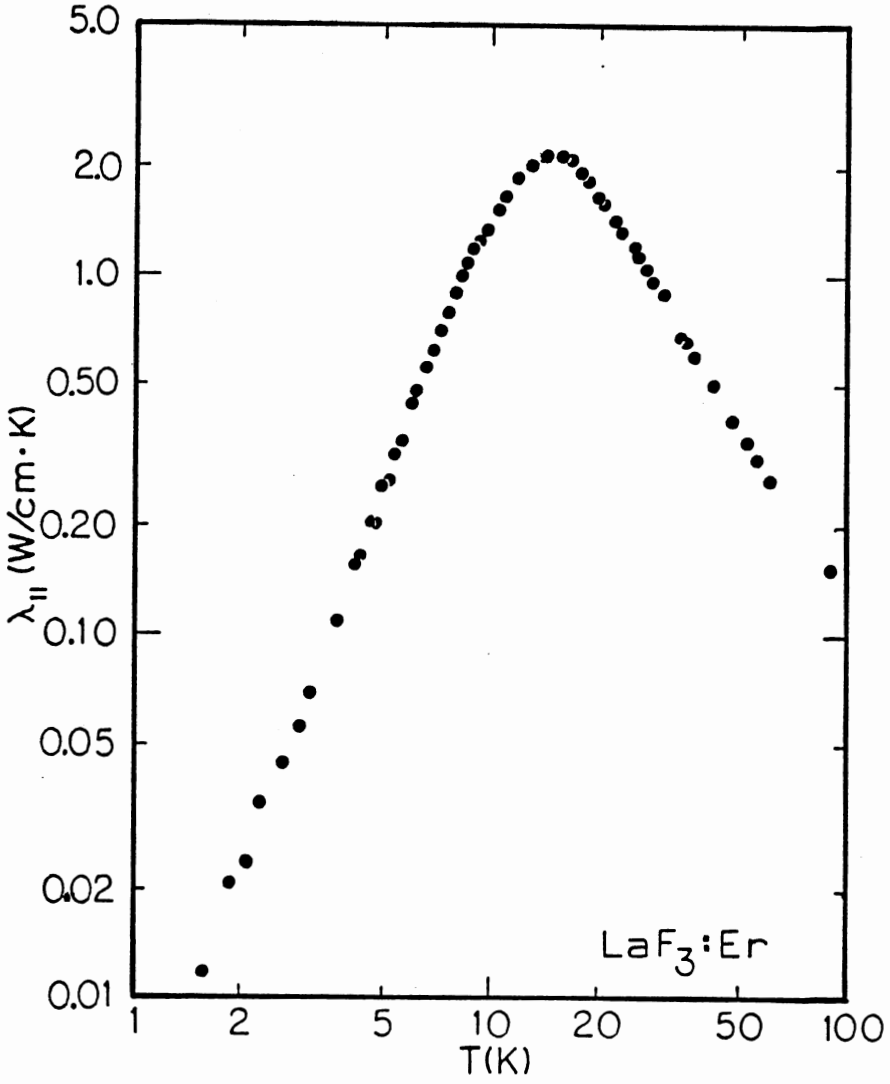

Figure 14. Thermal Conductivity of LaF_3:0.1%Er^{3+} Parallel to the C-axis

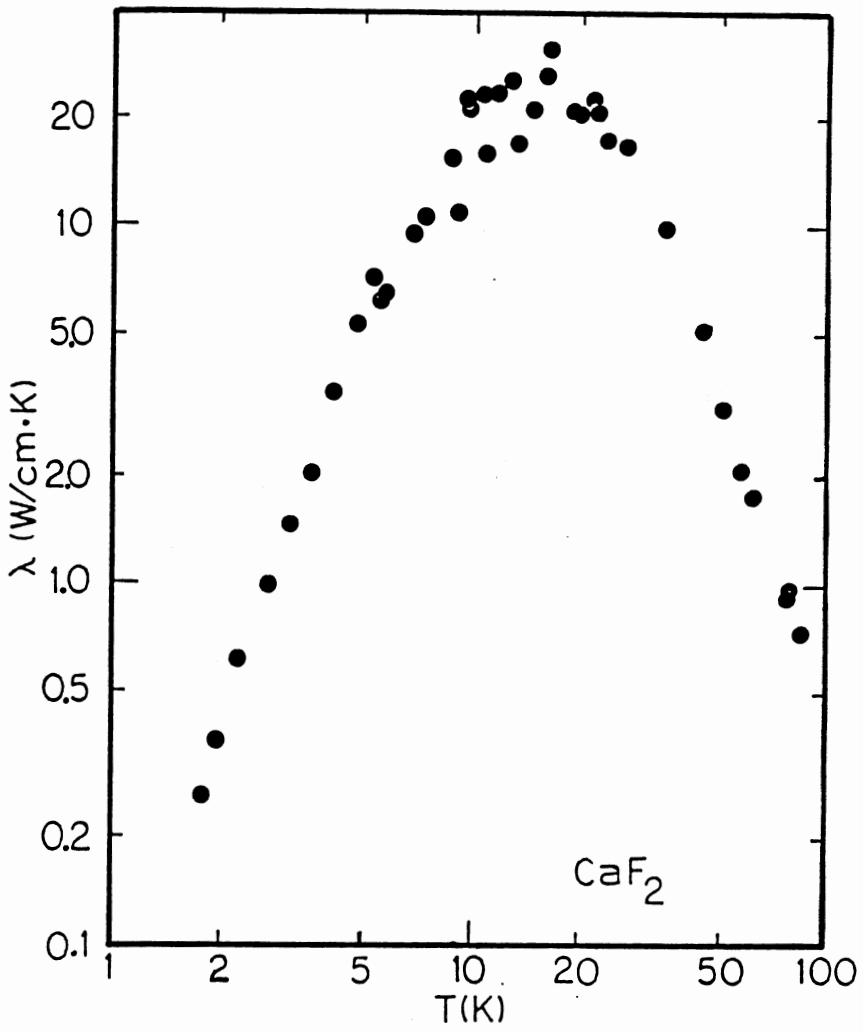

Figure 15. Thermal Conductivity of CaF_2

monicity parameter from the high temperature thermal conductivity. A semi-empirical expression by Slack [33] for the high temperature thermal conductivity of a crystal having r atoms per unit cell, contains this parameter:

$$\lambda = 3X10^{-8} \frac{\bar{M}_a a_o \Theta_D^3}{T\gamma^2 r^{2/3}} \tag{65a}$$

where $\bar{M}_a$ is the average atomic mass, a_o^3 the unit cell volume in $Å^3$, and T is the temperature. A similar equation is obtained theoretically by Raufosse and Klemens [34] from theoretical considerations also relates γ to λ:

$$\lambda = \frac{3^{1/3} k^3}{2^{1/6} \pi^{4/3} \gamma^2 \hbar^3} \bar{M}_a a_o \frac{\Theta_D^3}{T} . \tag{65b}$$

where k is Boltzman's constant.

Both these relations anticipate a thermal conductivity which behaves as 1/T at high temperatures. In this work, the $\lambda_\perp$ of LaF_3 goes as $T^{-1.6}$ and $\lambda_\parallel$ goes as $T^{-1.5}$ between 30 and 80K and λ for CaF_3 goes much faster in this temperature range because the 1/T dependence is expected to occur at and above the Debye temperature. Since the Debye temperature for LaF_3 and CaF_2 as obtained from specific heat measurements ([12] for LaF_3 and [35] for CaF_2) are about 400 K, and 500 K respectively, the temperature dependence in the liquid nitrogen range is stronger than T^{-1} as it is for most other crystals.

Nevertheless, calculations of γ for T = 100K are shown in Table IV, and give approximate values. Slack's equation for LaF_3 reduces to

$$\gamma^2 = 3.6X10^{-9} \frac{\bar{M}_a a \Theta_D^3}{\lambda T}$$

and equation (65b) becomes

TABLE V

GRÜNEISEN PARAMETER ESTIMATIONS

	$\bar{M}a$ (amu)	a (Å)	λ (K)	T (mW/cmK)	Θ_D (K)	γ_1	γ_2
LaF_3	49	6.56	130	100	400	2.4	2.6
LaF_3	49	6.56	60	100	400	3.5	3.8
CaF_3	26	5.46	500	100	500	2.4	2.4

γ_1 - Eq. (43).

γ_2 - Eq. (44).

$a = V_o^{1/3}$ for LaF_3 (but probably should use actual cell dimensions).

$$\gamma^2 = 4.2X10^{-9} \frac{\bar{M}_a a\theta_D^3}{\lambda T}$$

where $\bar{M}_a$ is in a.m.u., a is in A, and λ is in Watts/cmK. For CaF_3 equation (65a) r = 3, and

$$\gamma^2 = 1.44 \times 10^{-8} \frac{\bar{M}_a a\theta_D^3}{\lambda T}$$

and equation (65b) is

$$\gamma^2 = 1.68 \times 10^{-8} \frac{\bar{M}_a a\theta_D^3}{\lambda T}.$$

The general relaxation time used in our Debye integral (43) can be written

$$\tau^{-1} = v/L + A\omega^4 + [B_1 + B_2 e^{-\theta/aT}]\omega^4 T + D\omega \qquad (66)$$

where the first term on the right hand side represents the boundary scattering, the next term the point defect or Rayleigh term, the terms in brackets the "Normal" and "Umklapp" phonon-phonon scattering, and the last term accounts for scattering by static dislocations.

The boundary scattering term has no intrinsic frequency or temperature dependence and allows the thermal conductivity integral to take on the temperature behavior of the specific heat at the lowest temperatures. The parameter L, called the Casimir length, is obtained from the sample dimensions ℓ_1 and ℓ_2 of the rectangular cross-sectional area oriented perpendicular to the heat flow. For all three samples $L = 2/\sqrt{\pi}(0.3cm) = 0.34$ cm. The average velocity of sound for LaF_3 taken from Table I is $\bar{v} = 3 \times 10^5$ cm/s giving for boundary scattering the value $\tau = 1.17 \times 10^{-6}$s and $\tau = 8.26 \times 10^{-7}$s for CaF_2 for $\bar{v} = 4.1X10^5$cm/s, also from Table I.

The point defect scattering was estimated for $LaF_3:Er^{3+}$ for the

four isotopic masses of the erbium dopant. The isotopic scattering for lanthanum was ignored, its components being in the ratio of 0.09 / 99.91. Fluorine has only one known stable isotope. Calcium has six stable isotopes in the ratio of 96.9410: 0.647: 0.135: 2.086: 0.004: 0.187 for masses 40, 42, 43, 44, 46, and 48 respectively. Only the 2% of mass 44 amu produced appreciable isotopic scattering. Theoretical estimates of the point defect scattering are given by Klemens [36] and Slack [33].

$$\tau^{-1} = A\omega^4 \text{ where } A = \frac{a_o^3 \Gamma}{4\pi v^3} \tag{67}$$

where only mass defect scattering is considered. C_p is the concentration of defect p and ΔM_p is the mass variation from the average mass M. For a complex many atom crystal the term Γ becomes, for a crystal form $A_mB_n\ldots$

$$\Gamma = \frac{m}{m+n+\ldots}\left(\frac{Mm}{\overline{M}}\right) \Gamma_m + \frac{n}{m+n+\ldots}\left(\frac{Mn}{\overline{M}}\right)^2 \Gamma_n + \ldots \tag{68}$$

where

$$\Gamma_m = \Sigma\, C_p^{(m)} \left(\frac{\Delta M_p(m)}{\overline{M}_m}\right)^2, \text{ etc.} \tag{69}$$

and

$$\overline{M} = \frac{mM_m + nM_n + \ldots}{n + m + \ldots} \tag{70}$$

Appendix D details the point defect term for LaF_3 and gives

$$\tau^{-1} = 1.85 \times 10^{-46}\omega^4 \tag{71}$$

and for CaF_2

$$\tau^{-1} = 1.51 \times 10^{-44}\omega^4 \tag{72}$$

The deviation of the LaF_3 curves from T^3 behavior at low temperatures leads us to include a term for additional scattering. It is thought that static dislocation limited thermal conductivity should go as T^2. In fact, we found that a term of the form $\tau^{-1} = D\omega$ as suggested by Nabarro [37], was necessary to fit the low temperature points.

The parameter $D = N_D \frac{\gamma^2 B^2}{2\pi}$ and, although an estimate for the Burgers vector B and the Grüneisen parameter, γ, may be made, we have no estimate for the dislocation density. Thus, the D parameter obtained from the fit gave an estimate of the dislocation density for the LaF_3 samples. The thermal conductivity for CaF_2 behaved as T^3 and no additional term was required to obtain a fit.

The phonon-phonon scattering terms used in this study were derived in Chapter II and have the forms

$$\tau_N^{-1} = B_1 \omega^4 T \qquad \text{(Normal)} \qquad (73a)$$

$$\tau_u^{-1} = B_2 \omega^4 T e^{-\Theta/2T} \qquad \text{(Umklapp)} \qquad (73b)$$

The same form, except for the exponential cutoff factor in the Umklapp term, was used for both "Normal" and Umklapp scattering.

The "Umklapp term" doesn't necessarily represent entirely Umklapp scattering effects as scattering of all kinds increases with temperature, and the term really represents a sort of phenomenological low temperature cutoff which affects the mean free path for temperatures less than Θ/a where a is also a fitting parameter normally having a value of 2 to 5.

The normal scattering term, though, was related to the anharmonic decay rates obtained from the monochromatic phonon experiment described in Chapter II. The values obtained from Will, Eisfield and Renk [13]

for LaF_3 were

$$\tau^{-1} = 6.08 \times 10^{-58} \omega^5 \tag{74}$$

giving for the normal term, from Eq. (60)

$$B_1 = 68(1.31 \times 10^{11})(6.08 \times 10^{-58})$$

$$= 5.4 \times 10^{-45}$$

And for CaF_2, Baumgartner et al. [31] we found

$\tau^{-1} = 5.65 \times 10^{-60} \omega^5$ so that B_1 for CaF_2 becomes

$$B_1 = 68(1.31 \times 10^{-11})(5.65 \times 10^{-60}) \tag{75}$$

$$= 5.0 \times 10^{-47}$$

These estimates were used to guess the magnitude (except for the dislocation term) of the scattering when initiating the fitting procedure, and in the next section, the results of the actual fits obtained will be compared to these estimates.

Computation of the Numerical Fits

The integral of (43) using the relaxation time of equation (66) was performed numerically with a homemade Gaussian integration program using 16 sampling points (16-point Gaussian). The calculations were performed on a Hewlett-Packard Integrated Personal Computer. The program displayed the parameters selected, plotted the points on a screen and graphed the integrated thermal conductivity curve as a function of T as it was being calculated. Convergence of the routine was checked by comparing 16-point quadrature to 12, 8, and 4 point quadrature. There was

no discernable difference between the 16-, 12-, and 8-point programs, but the 4-point quadrature underestimated in the low temperature region and overestimated in the high temperature region. Table VI displays the results of the fitting parameters and Figures 16, 17, and 18 show the fits compared to the experimental data.

The point defect scattering for LaF_3 is from ~5 to 10 times larger than predicted, indicating that there are more point mass inhomogeneities present than those due to the isotopes accounted for. The boundary scattering discrepancy indicates that the mean free path of the phonons at the lowest temperatures is only 0.025 cm or so rather than the value 0.294 cm expected. This together with the necessity of having to introduce a $\tau^{-1} = D\omega$ term to obtain the proper temperature dependence suggests the presence of dislocations. Grain boundaries are another possible cause of smaller-than-expected mean free paths but evidence or grains would have showed up in the neutron scattering experiments done on this sample (5). If the Burgers vector is taken to be a lattice spacing (~7×10^{-8} cm), the dislocation density turns out to be 1.3×10^{10} disl/cm^2 for $\lambda_{\parallel}$ and 2.6×10^{10} disl/cm^2 for $\lambda_{\perp}$. The fact that the dislocation scattering is different in the two directions seems to indicate that the defects are be preferentiably oriented. This feature has been observed by Hudson [9] in his measurements of the thermal conductivity of LaF_3 samples grown without any special care to avoid impurities. He noted that the low temperature behavior of the $\lambda_{\perp}$ measurements went as $T^{2.1}$ whereas the $\lambda_{\parallel}$ measurements went as $T^{2.85}$. This is to be compared to 2.2 and 2.6, respectively, in our samples. The defects in his samples were not thought to be dislocations, but rather colloids of oxygen, in the form of hexagonal platelets lying parallel to

TABLE VI

PARAMETERS OF THE FIT

	ν/LF (s^{-1})	A (s^3)	B_1 (s^3/k)	B_2 (s^3/k)	Θ/a (*)	D (*)
$LaF_3:\lambda$						
Numerical	$1.0X10^{7}$	$1.00X10^{-45}$	$1.0X10^{-45}$	$2.3X10^{-43}$	90	$8X10^{-6}$
Calculated	$8.5X10^{5}$	$1.85X10^{-45}$	$5.4X10^{-45}$	---	90	---
$LaF_3:\lambda$						
Numerical	$1.5X10^{7}$	$5.00X10^{-44}$	$4.0X10^{-45}$	$7.0X10^{-43}$	75	$15X10^{-6}$
Calculated	$8.5X10^{3}$	$1.85X10^{-46}$	$5.4X10^{-45}$	---	90	---
$CaF_2:\lambda$						
Numerical	$1.8X10^{6}$	$8.00X10^{-45}$	$6.4X10^{-47}$	$1.0X10^{-43}$	140	0
Calculated	$1.2X10^{6}$	$1.51X10^{-44}$	$6.4X10^{-47}$	---	--	---

* dimensionless

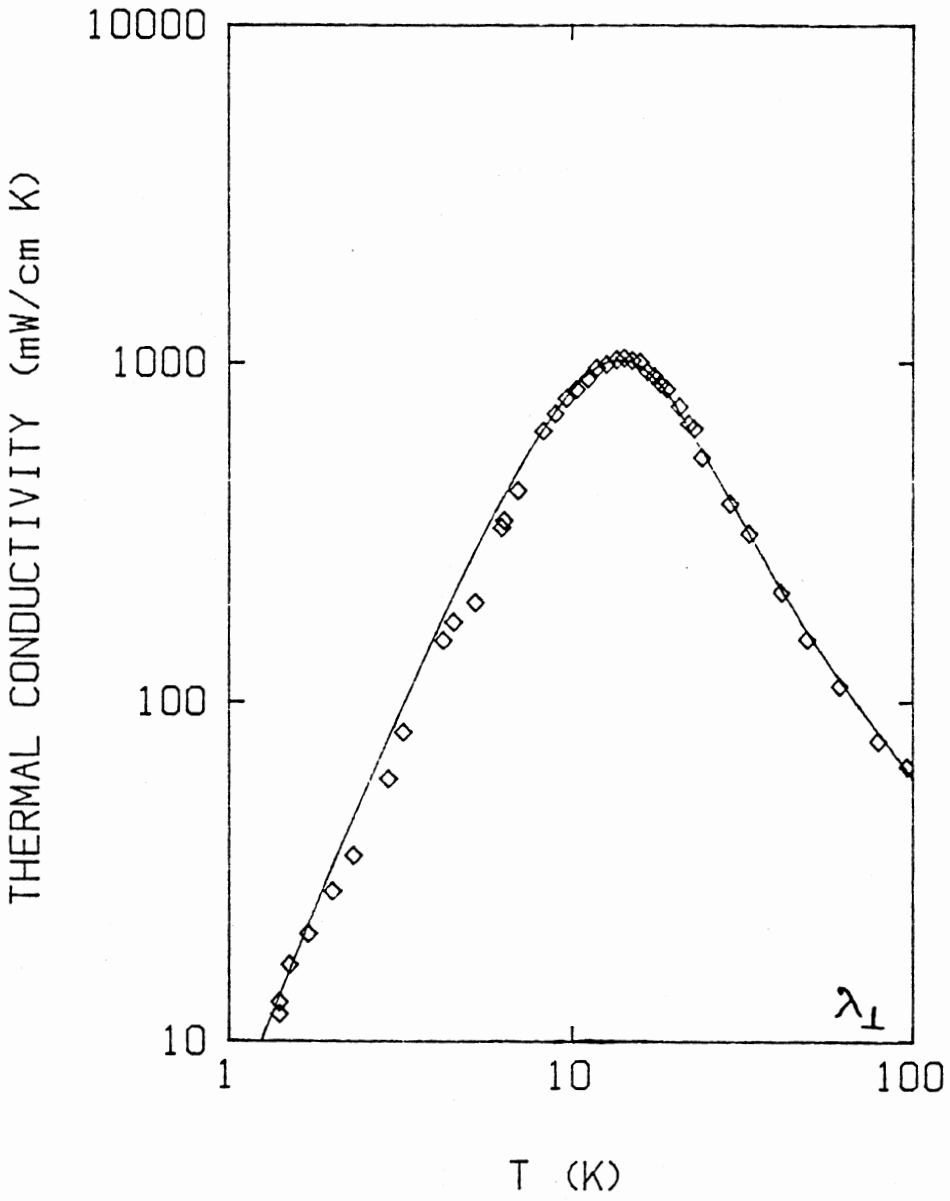

Figure 16. Numerical Fit for $\lambda_\perp$ (LaF_3)

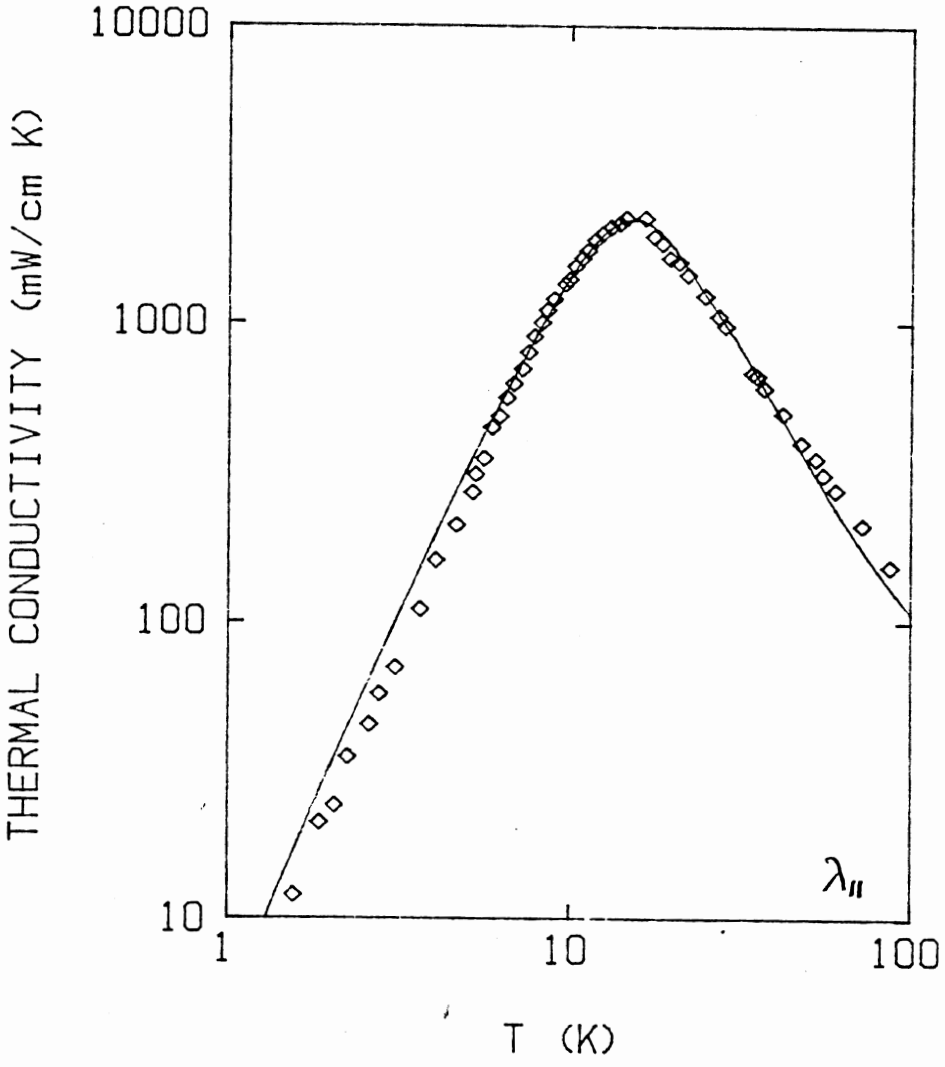

Figure 17. Numerical Fit for λ_{II} (LaF_3)

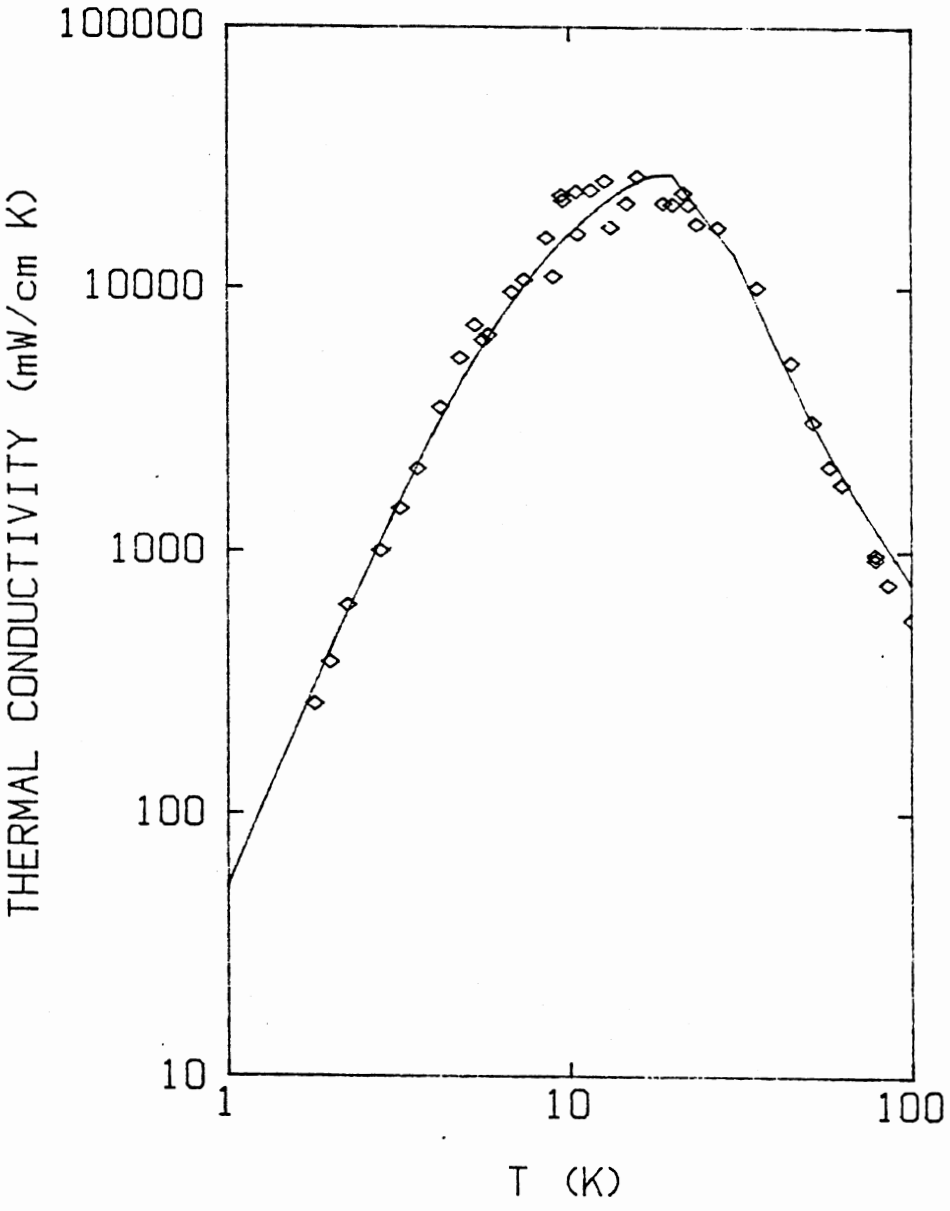

Figure 18. Numerical Fit for λ (CaF_2)

the basal planes as suggested by Mooney [38]. Previous measurements taken on pure samples of LaF_3 (Optovac) Hudson reports behavior of λ at low temperatures to be proportional to $T^{2.2}$.

The CaF_2 thermal conductivity fit required no term for dislocation scattering, and the point defect and boundary scattering terms are fairly close to the values expected for them.

The most striking feature of the modelling results is the comparable values of the predicted and the fitted anharmonic phonon scattering parameters. For LaF_3, the predicted value is within a factor of 1.35 for λ and a factor of 5.4 for λ and for CaF_2, the fitted and predicted values are essentially the same. Considering the fact that results from monochromatic phonon experiments are compared to results from thermal experiments, the agreement is certainly better than could have been expected. This suggests that phonons in the thermal environment scatter as $\tau^{-1} = B\omega^4 T$. It is surprising also that this form allows the fitting of the higher temperature data, rather than having to resort to the $\tau^{-1} = B\omega^2 T$ form suggested by Roufousse and Klemens [34] and normally used in the literature.

The Umklapp strengths are not predictable from other considerations and, along with the exponential term, represent, in a rather phenomenological way, the appearance of a broader range of phonon scattering with temperature. One aspect does deserve mention, though, and concerns the fact that the exponential term tends to allow the phonon scattering to emerge at a temperature of around 75 to 90 K for LaF_3. In the Introduction, attention was drawn to the low-lying optical mode that extends across the LaF_3 Brillouin zone. The average energy of this optic mode is around 40 cm^{-1} having a frequency of about 1.25 THz. The mode is

relatively flat, that is, its group velocity is so low that its contribution to thermal transport is nearly negligible. Since its density of states is high, though, it could serve as an effective scatterer of acoustic phonons which do carry the heat current; and such scattering would be strongest for acoustic phonons in the frequency range of 1-1.5 THz. Such phonons would be the dominant heat carrying phonons in a distribution peaking at a temperature of $T \sim \frac{\hbar\omega_o}{k} = 95°$.

The fit to the experimental data tends to overestimate the data for both $\lambda_{||}$ and $\lambda_{\perp}$ of LaF_3 in the low temperature region. That this is a consequence of some scattering mechanism in the 2 to 4 K range rather than a consequence of experimental error is not known. One plausible scattering mechanism for phonons in this temperature range might be a spin-phonon interaction within the manifold of the Er^{3+} levels. The splitting is 50 cm^{-1} and is much too large for resonant phonon absorption in this temperature range. Also, the absence of dips in the conductivity suggests that no direct spin-phonon interaction occurs, but it is possible that at these energies phonon-phonon scattering may rapidly mix different frequencies and wash out the expected dip. Nevertheless, a second-order, or Raman-type process might occur, scattering a broader range of phonons more weakly than a direct process. The phonon scattering rate is theoretically predicted [39] to be of the form

$$\tau^{-1} = \frac{3\pi C\varepsilon^4\omega_o\omega^4}{2\omega_D^3(\omega^2-\omega_o^2)^2} = \frac{E\omega_o^4\omega^4}{(\omega^2-\omega_o^2)^2} \qquad (76)$$

where C is the concentration of spins, ε is a dimensionless spin-phonon coupling parameter, ω_D is the Debye frequency, and ω_o the resonant phonon frequency of the spin level splitting. Such a term, however, was not included in the analysis here.

TABLE VII

PARAMETERS OF THE FITS FOR FIVE TECHNOLOGICALLY IMPORTANT CRYSTALLINE MATERIALS

	L/V	A (s^3)	B_1 (s^3K^{-1})	B_2 (s^3K^{-1})	Θ/α (K)
YAG	$7.88X10^{-7}$	$1X10^{-45}$	$2X10^{-45}$	$1X10^{-43}$	175
YIG	$4.8X10^{-8}$	$5X10^{-45}$	$5X10^{-45}$	$1X10^{-43}$	100
GaAs	$1.6X10^{-6}$	$1X10^{-45}$	$1.5X10^{-45}$	$2X10^{-44}$	70
SiO_2	$4.8X10^{-7}$	$5X10^{-45}$	$5X10^{-47}$	$1X10^{-43}$	70
Al_2O_3	$4.5X10^{-7}$	$1X10^{-47}$	$1X10^{-48}$	$7X10^{-45}$	250

TABLE VIII

PREDICTED ANHARMONIC DECAY RATE STRENGTHS

	$C_{thermal}$ (s^3/μ)	$C_{monochromatic}$ (s^4)
Al_2O_3	1×10^{-10}	11.2×10^{-60}
SiO_2	5.0×10^{-47}	5.6×10^{-60}
GaAs	1.5×10^{-45}	1.7×10^{-58}
YAG	2.0×10^{-45}	2.2×10^{-58}
YIG	5.0×10^{-45}	5.6×10^{-58}

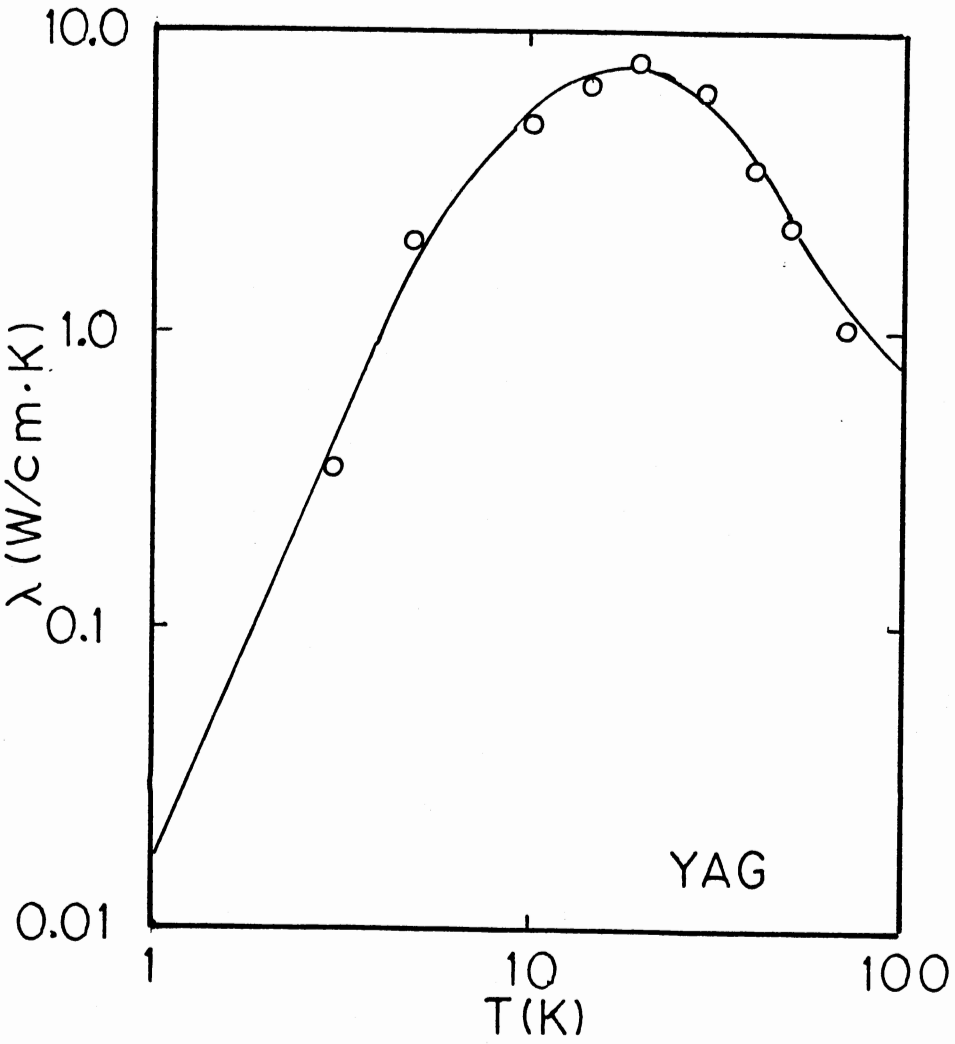

Figure 19. Numerical Fit for Yttrium Aluminum Garnet
(Points taken from reference 40)

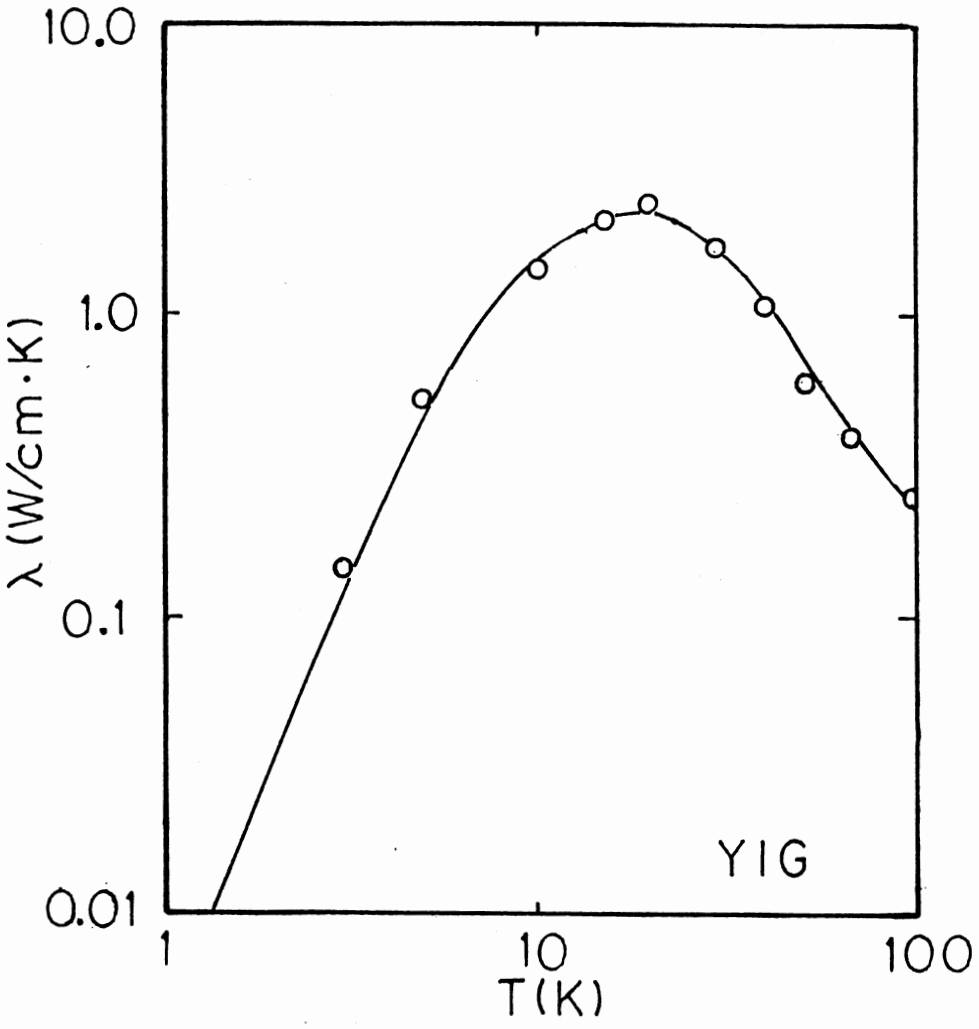

Figure 20. Numerical Fit for Yttrium Iron Garnet
(Points taken from reference 40)

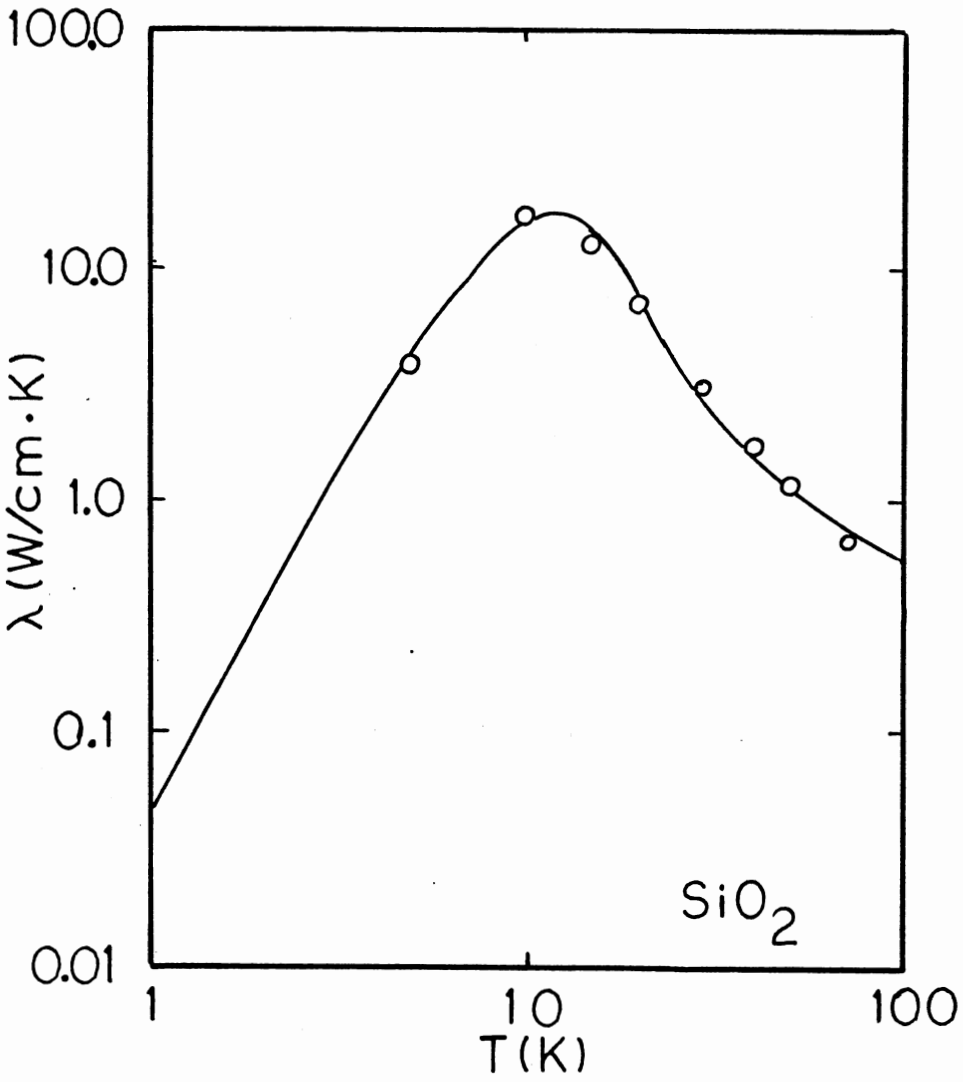

Figure 21. Numerical Fit for Quartz
(Points taken from
reference 17)

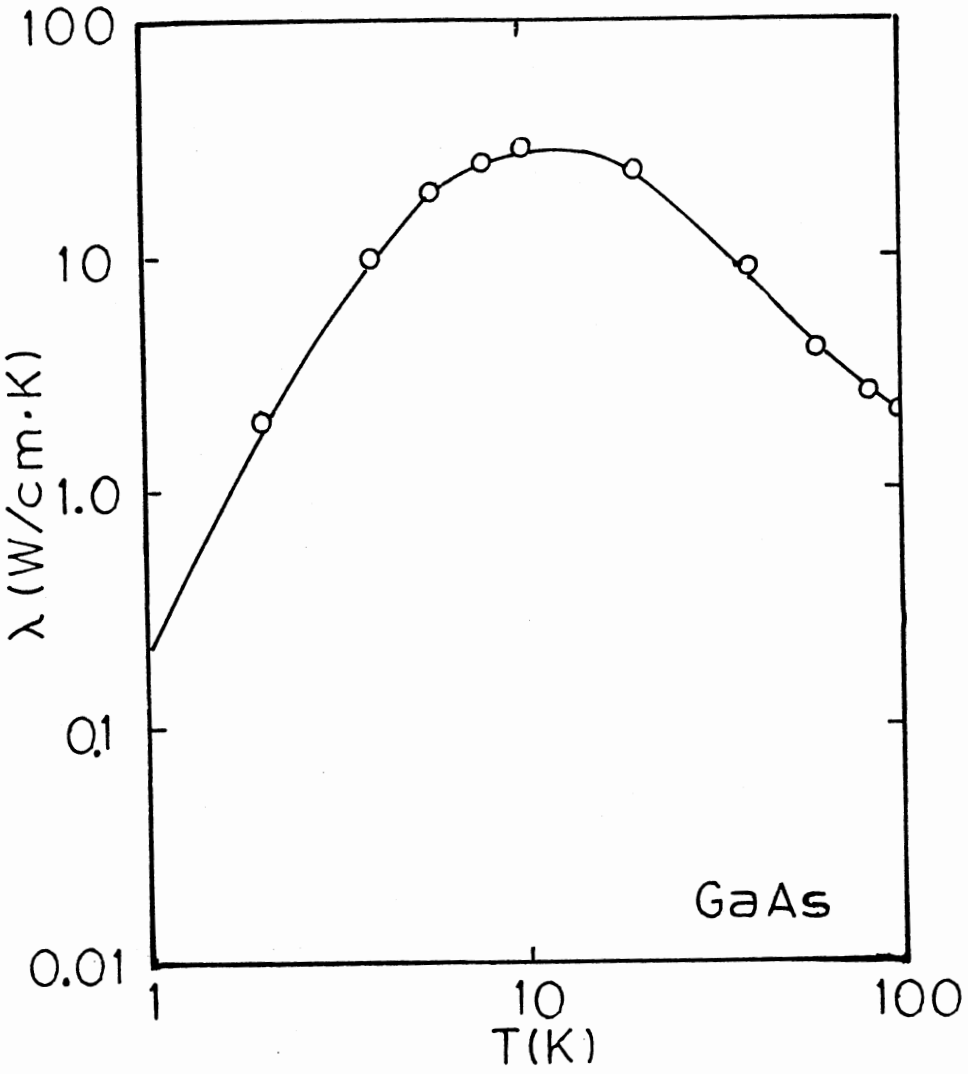

Figure 22. Numerical Fit for Gallium Arsenide
(Points taken from reference 41)

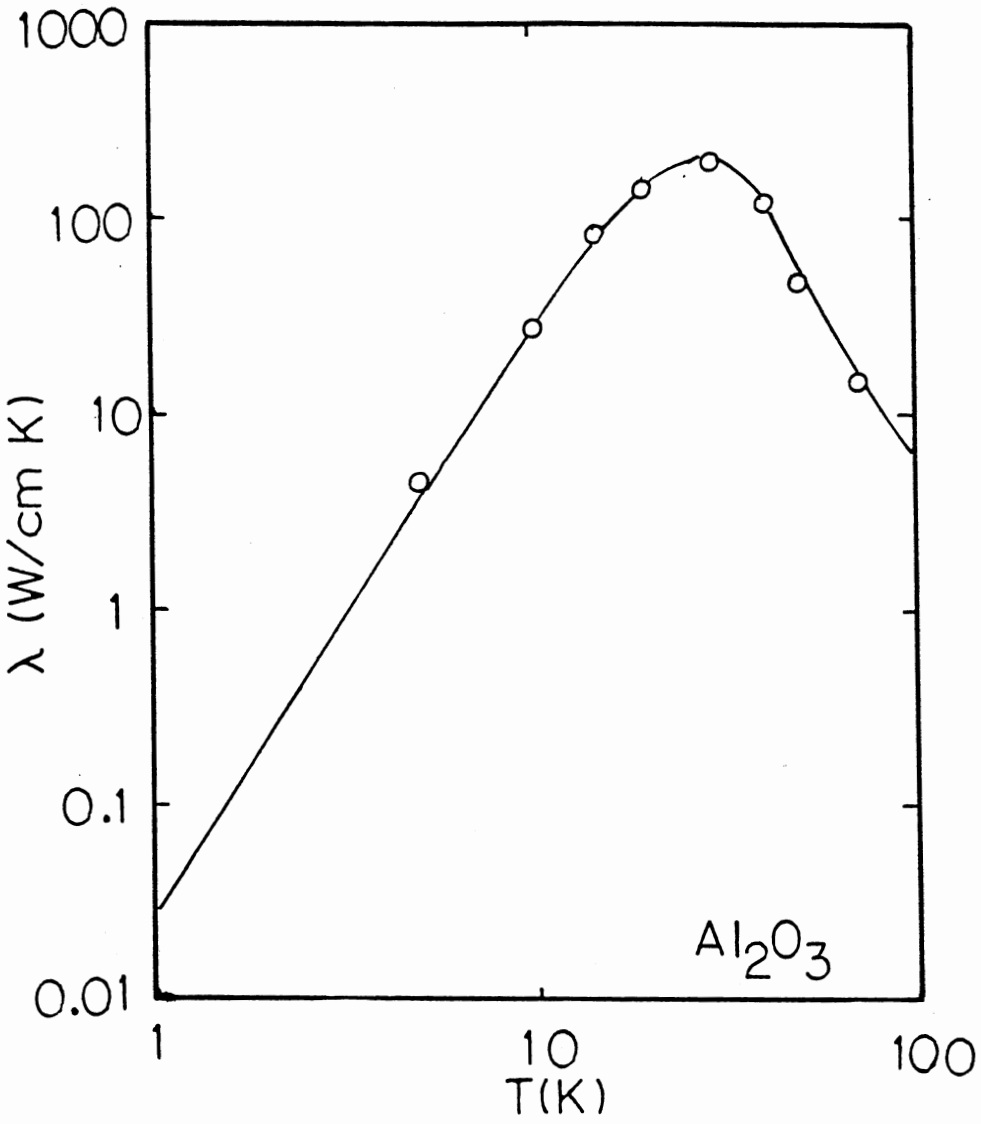

Figure 23. Numerical Fit for Aluminum Oxide
(Points taken from reference 17)

CHAPTER V

CONCLUSIONS

Practically all the features of the thermal conductivity which can be accounted for by the model employed here have met with satisfactory agreement, certainly qualitatively, and no significant inconsistencies arose from the quantitative treatment. One major point of this work was to suggest, because of the satisfactory comparison of our results with spectroscopic phonon experiments, that the form $\tau^{-1}_{phonon} = B\omega^4 T$ might be the correct one to be employed in thermal conductivity analysis, rather than the somewhat more phonomenological ones previously used. Certainly, one might look again at previous thermal conductivity measurements in the manner of this study, and predict what the anharmonic decay rates would be for other materials. In fact, we have done this for several materials, and the results are shown in Tables VII and VIII and Figures 19-23.

No resonant scattering was observed to be attributed to the optic mode, the effect of which was taken into account with a somewhat indirect argument concerning the phonon scattering horizon at around 90K.

Perhaps more careful low temperature studies, particularly in the presence of a magnetic field, would resolve the question of whether second-order phonon Raman scattering occurs in LaF_3.

Further studies on the anharmonic decay rates of monochromatically monitored phonon induced luminescence are indicated, especially on

materials whose thermal properties are well characterized. Such information might be useful technologically as well as scientifically, for example, if one wished to engineer a laser based on employing phonon assisted energy transfer the phonon decay rates would suggest what doping levels would be necessary to achieve this, and might be obtained from existing thermal conductivity data.

In conclusion, it should be stated that although the energies of the phonons monitored in the lifetime experiments [13], [31], were sharp, the phonons were mixed in mode, polarization and somewhat in direction, so that some averaging occurs even there, and maybe a portion of the agreement lies buried there.

BIBLIOGRAPHY

1. I. Oftedal. Z. Physick. Chem. 6, 272 (1929).
2. A. Zalkins, D. H. Templeton, and T. E. Hopkins, Inor. Chem. 5, 1466 (1964).
3. M. Mansmann, Z. Krist. 122, S375 (1965).
4. D. Gregson, et al., Acta Cryst. B39, 687 (1983).
5. G. S. Dixon and R. M. Nicklow, Sol. St. Comm. 47, 877 (1983).
6. P. R. W. Hudson, J. Phys. C. 9, L39 (1976).
7. P. H. Klein and W. J. Croft, J. Appl. Phys. 38, 1603 (1967).
8. W. G. Lyon, et al., J. Chem. Phys. 69, 167 (1978).
9. P. R. W. Hudson J. Phys. C. 9, L43.
10. R. Laiho, M. Lakkisto, and T. Levola, Phil. Mag. A, 47, 235 (1983).
11. C. Krischer, Appl. Phys. Lett. 13, 310 (1968).
12. E. F. Westrum, Jr. and A. F. Beale, Jr., J. Phys. Chem. 65, 353 (1961).
13. J. M. Will, W. Eisfeld, and K. F. Renk, Appl. Phys. A 31, 191 (1983).
14. M. M. Elcombe and A. W. Pryor, J. Phys. C., 3, 492 (1970).
15. G. A. Slack, Phys. Rev. 122, 1451 (1961).
16. A. K. McCardy, H. J. Maris, and C. Elbaum, Phys. Rev. B 2, 4077 (1970).
17. Y. S. Touloukian, R. W. Powell, C.Y. Ho, and P. G. Klemens, "Thermal Conductivity of Nonmetallic Solids", Thermophysical Properties of Matter 2, JFJ/Plenum, New York (1970).
18. R. W. G. Wycoff, Crystal Structures, Vol. 2, Interscience, New York (1963).
19. R. E. Peierls, Quantum Theory of Solids, Chapter 2, (Oxford University Press, Oxford, 1955).

20. W. E. Bron, Rept. Prog. Phys. 43, 302 (1980).

21. J. M. Ziman, Electrons and Phonons, (Clarendon Press, Oxford, 1960).

22. A. Matthiessen, Rep. Br. Assoc. 32, 144 (1862).

23. R. Berman, Thermal Conduction in Solids, p.69-72, (Oxford Univ. Press, Oxford, 1976).

24. J. Callaway, Phys Rev. 113, 1046 (1958).

25. R. J. von Gutfeld and A. H. Nethercot, Phys. Rev. Lett. 12, 641 (1964).

26. C. H. Anderson and E. S. Sabisky, Phys. Rev. Lett. 18, 235 (1967).

27. W. E. Bron and E. Keilmann, Phys. Rev. B 12, 2496 (1975).

28. W. E. Bron, and W. Grill, Phys. Rev. B 16, 5315 (1977).

29. R. Orbach and L. A. Vredevoe, Physics 1, 91 (1964).

30. P. G. Klemens, J. Appl. Phys. 38, 4573 (1967).

31. R. Baumgartner, M. Englehardt, and K. F. Renk, Phys. Rev. Lett. 47, 1403 (1981).

32. W. E. Bron, Phys. Rev. B, 21, 2627 (1980).

33. G. A. Slack, Phys. Rev. 126, 427 (1962).

34. M. Roufosse and P. G. Klemens, Phys Rev B 7, 5379 (1973).

35. D. R. Huffman and M. H. Norwood, Phys. Rev. 117, 709 (1960).

36. P. G. Klemens, Proc. Phys. Soc. 68, 1113 (1955).

37. F. R. N. Nabarro, Proc. R. S. London, Ser. A 209, 278 (1951).

38. J. B. Mooney, Infrared Phys. 6, 153 (1966).

39. G. A. Toombs and F. W. Sheard, J. Phys. C, 6, 1457 (1973).

40. G. A. Slack and D. W. Oliver, Phys. Rev. B 4, 592 (1971).

41. M. G. Holland, Phys. Rev. 134A, 471 (1964).

42. G. K. White, Experimental Techniques in Low-Temperature Physics, 3rd Ed., Oxford (1979).

APPENDIX A

CONDUCTIVE HEAT LOSS

The heat loss due to conduction is given by

$$\dot{Q} = \frac{\lambda A \Delta T}{\ell}$$

The major sources of error due to heat loss through conduction are losses through the four constantan lead wires from the gradient heater and thermal shunting by the gold jumper wire. Data relevant to the calculations are summarized below.

Material	No. of wires	dia. (cm)	area A $(cm)^2$	length l (cm)	λ (mW/cmK) (77K)	(10K)	(4.2K)	(2K)
Constantan	4	$1.3X10^{-2}$	$3.3X10^{-5}$	10	230	30	8	-
Gold (Fe)	1	$1.3X10^{-2}$	$3.3X10^{-5}$	10	3000	2000	500	200

Typical ΔT values for various temperature for the expermental conditions are:

	77K	30K	10K	4.2K	2K
Constantan	1	16	6	0	2
Gold (Fe)	1	0.05	0.1	0.1	0.05

APPENDIX B

ESTIMATION OF GRADIENT HEATER LOSS

DUE TO IMPERFECT VACUUM

A semi-empirical formula for heat loss due to imperfect vacuum (43) is

$$\dot{q} = 1.06 \frac{\gamma+1}{\gamma-1} a_o \frac{T_2-T_1}{\sqrt{M}} p$$

$$= 2.1 a_o p(T_2-T_1) \text{ W/M}^2 \quad \text{for helium}$$

$$= 1.2 a_o p(T_2-T_1) \text{ W/M}^2 \quad \text{for air}$$

where a_o = accommodation coefficient and will be taken as $a_o = 1$ (worst case), p is pressure in pascals, and T_2-T_1 the temperature difference between two surfaces, then, for helium as the exchange gas

If $p = 10^{-3}$ Pa and $\Delta T_{max} = 16K$, then if the heater has an area of $2.3 \times 10^{-4} m^2$

$$\dot{Q} = [(2.1)(10^{-3})(16K) \text{ W/m}^2](2.5 \times 10^{-4} m^2)$$

$$= 8.4 \mu W$$

APPENDIX C

RADIATIVE HEAT LOSS

Loss due to radiation can be estimated with the Stephan-Boltzmann Law

$$\dot{Q} = \tfrac{1}{2}\,\sigma A\varepsilon(T_2^4 - T_1^4) \quad \text{where } \sigma = 5.67 \times 10^{-7}\ \frac{mW}{cm^2 K}$$

If the heater is regarded to be a cylinder of radius 2mm and length 4mm, the radiative surface has area $A = 0.75cm^2$. If the emissivity, $\varepsilon = 1$ (worst case) then the radiative heat losses have the estimates below:

	$T_2 = 80K,\ T_1 = 77K$ (high temperature)	$T_2 = 20K,\ T_1 = 4K$ (low temperature)
$\dot{Q}$	2.47 mW	68μW
Error for 10mW input	25%	0.68%

The thermal conductivity tends to be measured as being larger than it actually is at higher temperatures.

APPENDIX D

POINT DEFECT CALCULATIONS

For Er^{3+} in LaF_3 let the formula be $L_{0.999}Er_{0.001}F_3$

$$\bar{M} = \frac{0.999(138.9)+0.001(167)+3(9)}{4} = 41.5$$

$$\Gamma_{Er} = 0.016\ (\frac{3}{167})^2 + 0.334\ (\frac{1}{167})^2 + 0.27\ (\frac{1}{167})^2 + 0.15\ (\frac{3}{167})^2$$

$$= 7.53\ X10^{-5}$$

$$\bar{M}_{Er} = 167$$

$$\Gamma = \frac{0.001}{4}(\frac{167}{41.5})^2(7.53\ X\ 10^{-5})$$

$$= 3.05\ X\ 10^{-7}$$

$$A = \frac{a^3\Gamma}{4\pi\bar{v}^3} = \frac{(4.6X10^{-23}cm^3)(3.05X10^{-7})}{4(3.14)(2.9X10^5)^3}$$

$$= 4.6\ X\ 10^{-47}$$

For Ca in CaF_2

$$\bar{M}_{Ca} = 39.97 \sim 40$$

$$\Gamma_{Ca} = 0.9494(0)^2 + (0.0209)\left(\frac{4}{40}\right)^2 + 0.0065\left(\frac{2}{40}\right)^2 = 2.25 \times 10^{-4}$$

$$\bar{M} = \frac{40+2(9)}{3} = 19.33$$

$$\Gamma = \frac{1}{3}\left(\frac{40}{19.33}\right)^2(2.25 \times 10^{-4}) = 3.21 \times 10^{-4}$$

$$A = \frac{a_o^3\Gamma}{4\pi v^{-3}} = \frac{(4.07\times10^{-23}\,cm^3)}{4(3.14)(4.1\times10^5)^3}(3.21\times10^{-4}) = 1.51 \times 10^{-44}\,s^3$$

APPENDIX E

TABULATION OF DATA FOR LaF_3:0.1% Er^{3+}

IN THE DIRECTION PARALLEL

TO THE C-AXIS

$\ell/A = 3.33\ cm^{-1}$

V_A (mV)	T (K)	I_H (mA)	V_H (V)	ΔV (μV)	dE/dT (μV/K)	ΔT (K)	λ (mW/cmK)
1.737	1.56	1.01	0.0408	0.07	6.56	0.011	12
1.734	1.86	1.50	0.0603	0.10	6.90	0.014	21
1.732	2.06	2.00	0.0803	0.16	7.20	0.022	24
1.730	2.25	2.50	0.1008	0.18	7.50	0.024	35
1.727	2.60	3.00	0.1209	0.22	8.04	0.027	45
1.725	2.78	3.50	0.1412	0.24	8.28	0.029	57
1.722	3.1	4.01	0.1618	0.27	8.80	0.031	70
1.717	3.66	5.02	0.2033	0.30	9.47	0.032	110
1.713	4.07	6.00	0.2430	0.31	9.96	0.031	160
1.707	4.67	7.03	0.2860	0.34	10.63	0.032	210
1.712	4.17	4.01	0.1616	0.13	10.07	0.013	170
1.708	4.57	5.02	0.2027	0.17	10.52	0.016	210
1.705	4.87	6.00	0.2427	0.21	10.83	0.019	260
1.702	5.2	6.50	0.2637	0.23	11.13	0.021	270
1.707	5.3	7.01	0.2842	0.25	11.23	0.022	310
1.697	5.6	7.50	0.3262	0.27	11.50	0.023	350
1.700	5.28	5.01	0.2028	0.11	11.32	0.01	340
1.697	5.6	6.02	0.2432	0.15	11.50	0.013	375
1.694	5.9	7.03	0.2847	0.18	11.80	0.015	445
1.690	6.2	8.04	0.3276	0.21	12.00	0.018	485
1.687	6.5	9.04	0.3717	0.24	12.20	0.020	560
1.683	6.8	10.00	0.4126	0.27	12.45	0.022	625
1.677	7.2	11.05	0.4549	0.30	12.78	0.024	700
1.674	7.5	12.01	0.4969	0.32	12.90	0.025	795
1.670	7.8	13.03	0.5392	0.34	13.08	0.026	900
1.665	8.2	14.03	0.5858	0.36	13.29	0.027	1000
1.660	8.5	15.02	0.6293	0.39	13.47	0.029	1100
1.655	8.9	16.05	0.6728	0.41	13.62	0.030	1200
1.650	9.3	17.05	0.7176	0.44	13.78	0.032	1250
1.646	9.6	18.01	0.7600	0.47	13.90	0.034	1350

V_A (mV)	T (K)	I_H (mA)	V_H (V)	ΔV (μV)	dE/dT (μV/K)	ΔT (K)	λ (mW/cmK)
1.641	9.9	19.03	0.8063	0.50	14.00	0.036	1400
1.636	10.3	20.03	0.8486	0.52	14.12	0.037	1550
1.633	10.5	21.01	0.8921	0.55	14.18	0.039	1600
1.629	10.8	22.01	0.9363	0.58	14.28	0.041	1650
1.623	11.2	23.03	0.9832	0.61	14.35	0.043	1750
1.619	11.5	24.02	1.032	0.63	14.41	0.044	1900
1.614	11.8	25.03	1.071	0.68	14.47	0.047	1900
1.610	12.1	26.02	1.1154	0.72	14.51	0.050	1950
1.605	12.4	27.03	1.1616	0.75	14.56	0.052	2000
1.500	12.8	28.03	1.2063	0.80	14.61	0.055	2050
1.596	13.1	29.02	1.2508	0.84	14.63	0.057	2100
1.590	13.5	30.04	1.2973	0.88	14.66	0.060	2150
1.584	13.9	31.03	1.3413	0.94	14.67	0.064	2160
1.581	14.1	32.01	1.3843	0.99	14.69	0.067	2200
1.576	14.5	15.01	0.6232	0.21	14.70	0.014	2250
1.561	15.5	15.01	0.6273	0.21	14.71	0.014	2250
1.547	16.5	15.01	0.6293	0.22	14.67	0.015	2100
1.532	17.5	15.02	0.6306	0.23	14.61	0.016	1950
1.516	18.5	15.04	0.6324	0.25	14.50	0.017	1850
1.504	19.5	15.06	0.6281	0.27	14.40	0.019	1650
1.487	20.7	15.06	0.6326	0.29	14.25	0.020	1600
1.468	22.0	15.01	0.6342	0.31	14.06	0.022	1450
1.455	22.9	15.10	0.6378	0.33	13.85	0.024	1350
1.441	23.9	15.00	0.6349	0.34	13.77	0.025	1250
1.430	24.7	15.06	0.6384	0.36	13.62	0.026	1230
1.417	25.6	15.02	0.6371	0.38	13.46	03028	1150
1.400	27.1	15.00	0.6371	0.40	13.35	0.030	1050
1.381	28.4	15.06	0.6109	0.43	13.04	0.033	975
1.364	29.8	15.11	0.6431	0.46	12.80	0.036	900
1.307	34.0	14.99	0.6403	0.57	12.15	0.047	680
1.300	35.0	15.00	0.6405	0.58	12.07	0.048	665
1.281	36.8	15.03	0.6426	0.63	11.86	0.053	605
1.221	41.8	15.03	0.6430	0.73	11.23	0.065	495
1.161	47.3	15.02	0.6467	0.87	10.66	0.082	395
1.109	52.4	15.03	0.6468	0394	10.19	0.092	350
1.077	55.5	15.02	0.6471	1.04	9.90	0.105	310
1.030	60.5	14.94	0.6478	1.12	9.50	0.118	275

APPENDIX F

TABULATION OF DATA FOR LaF_3:0.01%Er^{3+}

IN THE DIRECTION PERPENDICULAR

TO THE C-AXIS

$\ell/A = 3.56\ cm^{-1}$ except where noted

V_A (mV)	T (K)	I_H (mA)	V_H (V)	ΔV (μV)	dE/dT (μV/K)	ΔT (K)	λ (mW/cmK)
1.7368	1.22	0.25	0.0117	0.025	6.52	0.004	6.5
1.7356	1.36	0.50	0.0230	0.05	6.68	0.0075	13.1
1.7358	1.35	0.50	0.0230	0.055	6.62	0.0083	12
1.7340	1.51	0.77	0.0352	0.10	6.9	0.014	16
1.7328	1.66	0.98	0.0450	0.13	7.12	0.018	21
1.7303	1.91	0.50	0.0226	0.03	7.5	0.004	24
1.7298	1.96	0.75	0.0339	0.06	7.58	0.0079	28
1.7287	2.3	1.00	0.0458	0.09	8.04	0.011	35
1.7280	2.2	1.52	0.0698	0.20	7.88	0.025	36
1.7213	2.9	1.00	0.0450	0.06	8.86	0.0068	57
1.7189	3.2	1.50	0.0685	0.10	9.25	0.011	80
1.7081	4.2	3.00	0.1396	0.25	10.52	0.24	150
1.6852	6.3	5.00	0.2335	0.36	12.33	0.029	340
1.7045	4.5	5.01	0.2323	0.63	10.86	0.058	170
1.6982	5.2	3.01	0.1393	0.26	11.41	0.023	160
1.6870	6.2	4.02	0.1865	0.30	12.20	0.025	260
1.6771	6.8	5.00	0.2335	0.38	12.75	0.030	335
1.6604	8.3	6.00	0.2836	0.39	13.45	0.029	500
1.6517	8.9	7.00	0.3302	0.48	13.73	0.035	565
1.6415	9.6	8.00	0.3790	0.58	14.00	0.041	625
1.6312	10.3	9.00	0.4273	0.70	14.21	0.049	665
1.6203	11.1	10.02	0.4756	0.82	14.39	0.057	715
1.6096	11.8	11.00	0.5246	0.93	14.51	0.064	770
1.5980	12.6	12.00	0.5736	1.09	14.62	0.075	790
1.5867	13.5	13.00	0.0235	1.25	14.68	0.085	815
1.5754	14.2	14.00	0.6733	1.44	14.71	0.098	825
1.5637	15.0	15.01	0.7250	1.69	14.71	0.115	810
1.5526	15.8	16.00	0.7665	1.93	14.69	0.131	800
1.5410	16.6	17.01	0.7995	2.227	14.65	0.155	750
1.5295	17.4	18.00	(0.846)	2.62	14.59	0.179	730

V_A (mV)	T (K)	I_H (mA)	V_H (V)	ΔV (μV)	dE/dT (μV/K)	ΔT (K)	λ (mW/cmK)
1.5182	17.9	19.00	(0.893)	3.04	14.50	0.210	690
1.5070	18.9	20.00	(0.940)	3.48	14.44	0.241	565
1.5070	19.0	5.00	0.2375	0.17	14.43	0.012	860
1.4990	19.6	7.00	0.3333	0.34	14.35	0.024	840
1.4833	20.6	10.00	0.4806	0.79	14.22	0.056	740
1.4661	21.8	12.00	0.5796	1.27	14.04	0.090	660
1.4278	24.5	12.00	0.5802	1.55	13.61	0.114	520
1.3670	29.2	12.00	0.5851	2.02	12.86	0.157	380
1.3234	32.8	12.00	0.5881	2.38	12.30	0.193	315
1.2273	41.0	12.00	0.5932	3.28	11.29	0.290	210
1.1325	49.5	12.00	0.5986	4.20	10.43	0.406	155
1.0223	61.0	12.00	0.6023	5.27	9.42	0.559	111
			$\ell/A = 6.97 cm^{-1}$				
0.8359	82.0	7.46	0.1805	0.85	7.86	0.108	87
			$\ell/A = 5.96 cm^{-1}$				
0.8619	79.0	7.50	1.1820	0.87	8.05	0.111	74
			$\ell/A = 6.5 cm^{-1}$				
1.0167	61.4	10.06	0.2341	1.17	9.21	0.127	121
0.9438	69.6	10.03	0.2344	1.26	8.57	0.147	104
1.1047	52.6	10.04	0.2323	1.04	10.10	0.103	147
0.5381	127.	10.00	0.2374	1.68	5.62	0.299	52

APPENDIX G

TABULATION DATA FOR CaF_3

$\ell/A = 17.4\ cm^{-1}$

V_A (mV)	T (K)	I_H (mA)	V_H (V)	ΔV (μV)	dE/dT (μV/K)	ΔT (K)	λ (mW/cmK)
1.700	1.8	2.51	0.1173	0.12	6.1	0.019	260
1.738	2.0	5.06	0.2365	0.35	6.3	0.056	375
1.735	2.3	10.03	0.4735	0.91	6.68	0.136	610
1.730	2.75	15.01	0.7209	1.43	7.50	0.191	985
1.726	3.18	20.03	0.9736	1.88	8.15	0.231	1470
1.722	3.6	25.04	1.2346	2.26	8.70	0.259	2080
1.718	4.1	15.46	0.7488	0.55	9.34	0.0589	3400
1.709	4.8	20.02	0.9812	0.64	10.41	0.062	5550
1.700	5.6	19.96	0.9820	0.62	11.23	0.055	6100
1.698	5.8	24.97	1.241	0.96	11.61	0.82	6600
1.704	5.3	25.05	1.243	0.84	11.23	0.075	7200
9.686	6.8	19.95	0.9804	0.46	12.23	0.038	9100
1.679	7.4	21.16	1.0431	0.45	12.6	0.036	11000
1.663	8.6	21.45	1.0566	0.34	13.34	0.0255	15500
1.651	9.5	25.13	1.2464	0.33	13.74	0.024	22700
1.649	9.6	25.09	1.2468	0.35	13.78	0.025	21400
1.636	10.6	25.11	1.2467	0.33	14.12	0.023	23300
1.618	11.9	25.03	1.2462	0.33	14.42	0.023	23800
1.609	12.5	25.04	1.2480	0.31	14.53	0.021	25500
1.580	16.1	25.00	1.2456	0.26	14.71	0.018	30600
1.562	15.8	24.95	1.245	0.30	14.71	0.020	26500
1.666	8.4	15.02	0.7296	0.23	13.24	0.017	11000
1.637	10.5	15.02	0.7306	0.17	14.1	0.0121	15800
1.604	12.9	15.88	0.7746	0.18	14.57	0.012	17000
1.580	14.6	15.88	0.7765	0.15	14.70	0.010	21000
1.514	19.0	15.03	0.7356	0.13	14.50	0.009	21400
1.497	20.2	14.88	0.7304	0.13	14.35	0.009	20800
1.480	21.4	15.13	0.7432	0.12	14.2	0.0085	23000
1.471	22.0	15.13	0.7431	0.13	14.1	0.0092	21000
1.458	23.0	15.13	0.7439	0.16	14.00	0.011	17000
1.403	27.0	15.10	0.7457	0.16	13.30	0.012	16300
1.304	35.0	15.10	0.7514	0.24	12.12	0.020	10000
1.203	44.0	15.07	0.7565	0.42	11.02	0.338	5200
1.124	51.0	15.04	0.7561	0.67	10.33	0.65	3050
1.065	57.0	15.03	0.7593	0.92	9.79	0.094	2100
1.025	61.0	15.02	0.7583	1.05	9.45	0.111	1790

V_A (mV)	T (K)	I_H (mA)	V_H (V)	ΔV (μV)	dE/dT (μV/K)	ΔT (K)	λ (mW/cmK)
0.809	84.0	15.06	0.7695	2.05	7.62	0.269	750
0.701	100.0	15.06	0.7718	2.48	6.73	0.365	555
0.550	123.0	15.02	0.7725	2.91	5.71	0.510	400
0.8822	77.6	10.00	0.5080	0.78	8.21	0.095	930

APPENDIX H

VELOCITY AVERAGING CALCULATIONS

For LaF_3, the average velocity was calculated using

$$\frac{1}{\bar{v}^3} = \frac{1}{3}\left\{\frac{1}{\bar{v}_{ST}^3} + \frac{1}{\bar{v}_{FT}^3} + \frac{1}{\bar{v}_{L}^3}\right\}$$

where $\bar{v}_{ST}$ ($\bar{v}_{FT}$) was the arithmetic average of the slow (fast) transverse velocities for three directions in the crystal and $\bar{v}_L$ was the averaged longitudinal velocity, also arithmetic. The velocities used were obtained from the dispersion curve of LaF_3 [5], Figure 2. v_{ST} in the [100] direction is denoted $v_{ST}^{[100]}$, with likewise notation for the other modes and directions.

For Slow Tranverse modes

$$v_{ST}^{[110]} = 2.4 \times 10^5 \text{cm/s}$$

$$v_{ST}^{[100]} = 2.7 \times 10^5 \text{cm/s}$$

$$v_{ST}^{[001]} = 2.1 \times 10^5 \text{cm/s}$$

$$\bar{v}_{ST} = \frac{1}{3}\left\{v_{ST}^{[110]} + v_{ST}^{[100]} + v_{ST}^{[001]}\right\}$$

$\bar{v}_{ST} = 2.4 \times 10^5 \text{cm/s}$.

For Fast Transverse modes

$$v_{FT}^{[110]} = 2.8 \times 10^5 \text{cm/s}$$

$$v_{FT}^{[100]} = 3.2 \times 10^5 \text{cm/s}$$

$$v_{FT}^{[001]} = 2.1 \times 10^5 \text{cm/s}$$

$$\bar{v}_{FT} = 2.7 \times 10^5 \text{cm/s}.$$

For Longtitudinal modes

$$v_{L}^{[110]} = 6.0 \times 10^5 \text{cm/s}$$

$$v_{L}^{[100]} = 5.8 \times 10^5 \text{cm/s}$$

$$v_{L}^{[001]} = 6.2 \times 10^5 \text{cm/s}$$

$$\bar{v}_{L} = 6.0 \times 10^5 \text{cm/s}.$$

Thus

$$\bar{v}^{-3} = \frac{1}{3}\left[(2.4 \times 10^5)^{-3} + (2.7 \times 10^5)^{-3} + (6.0 \times 10^5)^{-3} \right]$$

$$\bar{v} = 3.0 \times 10^5 \text{cm/s for } LaF_3.$$

For CaF_2, the velocity calculation was simply taken to be

$$\frac{1}{\bar{v}^3} = \frac{1}{3}\left\{\frac{1}{v_{ST}^3} + \frac{1}{v_{FT}^3} + \frac{1}{v_L^3}\right\}$$

where

$$\bar{v}_L = 7.8 \times 10^5 \text{cm/s}$$

$$v_{FT} = 3.92 \times 10^5 \text{cm/s}$$

$$v_{ST} = 3.51 \times 10^5 \text{cm/s}$$

$$\bar{v} = 4.1 \times 10^5 \text{cm/s}.$$

VITA V

Wayne W. Vinson

Cadidate for the Degree of

Doctor of Philosophy

Thesis: THERMAL CONDUCTIVITY OF LaF_3:0.1%Er^{3+} FROM 1.8 K to 100K

Major Field: Physics

Biographical:

Personal Data: Born in Childress, Texas, March 17, 1949, the son of Ralph C. and Marion Vinson. Married to Cathy J. Chapman on August 23, 1970.

Education: Graduated from Springfield High School, Springfield, Oregon, in May 1967; received Bachelor of Science Degree in Physics from Panhandle State University in January, 1973; received Master of Science Degree from Oklahoma State University in May, 1977; completed requirements for the Doctor of Philosophy at Oklahoma State University in May, 1987.

Professional Experience: Teaching Assistant, Department of Physics, Panhandle State University, August, 1972, to December, 1973. At Oklahoma State University: Technical Assistant from June, 1974, to August, 1974; Teaching Assistant from September, 1974, to May, 1976. Physics Instructor at Cowley County Community College in Arkansas City, Kansas, from September 1978 to May, 1979. Returned to Oklahoma State University in September, 1984: Teaching Assistant from September, 1984, to August, 1986 and Instructor in Physics, September, 1986 to May, 1987.